PROCEEDINGS A

royalsocietypublishing.org/journal/rspa

Research

Cite this article: Ahern A, Thompson TB, Oliveri H, Lorthois S, Goriely A. 2025 Modelling cerebrovascular pathology and the spread of amyloid beta in Alzheimer's disease. *Proc. R. Soc. A* **481**: 20240548.
https://doi.org/10.1098/rspa.2024.0548

Received: 23 July 2024
Accepted: 3 February 2025

Subject Areas:
applied mathematics, mathematical modelling

Keywords:
Alzheimer's disease, cerebrovascular disease, prion, connectome, mathematical modelling, dynamical systems

Author for correspondence:
Alain Goriely
e-mail: goriely@maths.ox.ac.uk

Modelling cerebrovascular pathology and the spread of amyloid beta in Alzheimer's disease

Andrew Ahern[1], Travis B. Thompson[2], Hadrien Oliveri[3], Sylvie Lorthois[4] and Alain Goriely[1]

[1]Mathematical Institute, University of Oxford, Oxford, UK
[2]Department of Mathematics and Statistics, Texas Tech University, Lubbock, USA
[3]Max Planck Institute for Plant Breeding Research, Cologne, Germany
[4]Institut de Mécanique des Fluides de Toulouse, Université de Toulouse, CNRS, INPT, UPS, Toulouse, France

AG, 0000-0002-6436-8483

Alzheimer's disease (AD) is characterized in part by the accumulation and spread of amyloid beta proteins in the brain. Recent experiments have revealed that amyloid beta oligomers induce microvascular mural cells to contract, thereby constricting capillaries and increasing resistance to blood flow. Conversely, hypoperfusion promotes amyloid beta production and hinders its clearance, hence creating a pathogenic positive feedback loop. Here, we develop a mathematical model that combines protein–capillary interaction with the prion-like behaviour of amyloid beta. For sufficiently strong interaction, we find that healthy and diseased steady states, both stable, can exist simultaneously, implying that pathogenic protein seeds must exceed a critical threshold in order to trigger disease outbreak. We explore the consequences of this bistability for disease propagation through the brain's structural connectome network. Finally, in a first attempt to model the AD two-hit vascular hypothesis mathematically, we describe how spatially localized

Electronic supplementary material is available online at https://doi.org/10.6084/m9.figshare.c.7700081.

THE ROYAL SOCIETY PUBLISHING

deficits in blood supply, e.g. due to embolic stroke or atherosclerosis of the leptomeningeal vessels, may trigger disease outbreak and propagation.

1. Introduction

Amyloid beta and cerebral blood flow in Alzheimer's disease. A hallmark of Alzheimer's disease (AD) is the accumulation and spatial propagation of pathogenic forms of the amyloid beta (Aβ) protein in the brain [1]. Aβ is an intrinsically disordered protein [2] and can adopt conformational variants that assemble into abnormal aggregates, ranging in size from small oligomers to large, amyloidogenic fibrils [3,4]. Central to the toxicity of these misfolded forms of Aβ, as well as that of misfolded tau (τP), the other key pathogenic protein in AD, is their ability to induce misfolding in their normally folded counterparts via a prion-like mechanism [2,5–9], thereby giving rise to an inter-peptide infectious disease dynamics.

In addition to Aβ and τP accumulation, cerebrovascular pathology, such as cerebral amyloid angiopathy (CAA), is present in 80% of AD cases, prompting suggestions that it may contribute to the pathogenesis and/or aetiology of the disease [10–12]. Reduced cerebral blood flow (CBF) is the earliest biomarker of AD [13,14], and cerebrovascular disorders such as atherosclerosis and hypertension are established risk factors for the disease [15,16]. The cerebral vasculature has also been proposed as a potential target for disease-modifying therapies [10,17–21]. Moreover, in contrast to the nosology of the late twentieth century, which treated AD and vascular dementia (VaD) as intrinsically distinct [22–25], recent years have seen the concept of a mixed pathology, spanning a 'spectrum from "pure" AD … to "pure" VaD' [26], gain in prominence [17,26,27].

Aβ is a vasoconstrictive substance, and therefore diminishes CBF by increasing vascular resistance [28,29]. Recently, Nortley *et al.* [14] established that Aβ oligomers induce pericytes (mural cells that line the capillary bed; see figure 1b) to contract by activating the vasoconstrictor endothelin-1 (ET-1). In addition, Cruz Hernández *et al.* [32] showed that capillaries become occluded by circulating neutrophils at higher rates in AD than in health, possibly due to endothelial inflammation resulting from Aβ-induced oxidative stress.

Conversely, hypoxia upregulates Aβ production by promoting expression of BACE1 (β-site amyloid precursor protein (APP) cleaving enzyme 1) [33], and hypoperfusion following ischaemic injury causes overexpression and accumulation of APP [34,35]. Hypoperfusion may also diminish the brain's ability to clear Aβ across the blood-brain barrier (BBB) [30,36], the major clearance pathway of Aβ [20,37,38].

Positive feedback loop and the two-hit vascular hypothesis. A positive feedback loop between pathogenic Aβ accumulation and cerebral hypoperfusion has been hypothesised by biologists for twenty years (see [17, fig. 8], [14, fig. 6B], and [35, fig. 3]), consistent with the interactions described above. Additionally, the two-hit vascular hypothesis of AD states that cerebrovascular damage (hit 1)—due, for example, to atherosclerosis of intracranial vessels [15] or stroke [26,39]—is the initial trigger of Aβ accumulation (hit 2) in AD [20,36,40]. Though the positive feedback loop and the two-hit vascular hypothesis have been schematized in qualitative terms many times, they have not, to our knowledge, been formalized as mathematical models whose dynamical behaviours can be analysed.

Modelling of prion-like kinetics and vasculature in AD. The prion-like kinetics of Aβ, along with other proteins involved in neurodegeneration such as τP and α-synuclein, has been modelled mathematically for about 30 years [41–44], and with increased intensity over the past decade [45–51]. Key themes in these more recent studies are: (i) autocatalytic conversion of normal proteins into their pathogenic form, as discussed above, and (ii) spatial propagation of proteins, particularly trans-synaptic transport through the brain's structural connectome.

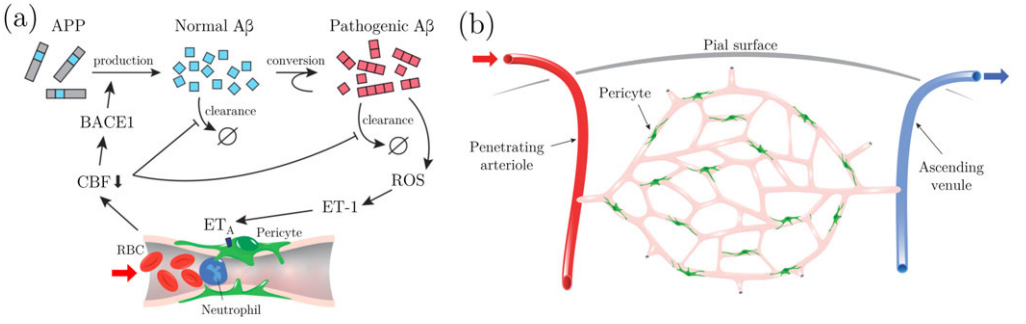

Figure 1. (a) Schematic of Aβ's prion-like kinetics and its interaction with capillary pericytes (cf. [30, fig. 3]). Normal Aβ is cleaved from the amyloid precursor protein (APP) by BACE1 and other enzymes, and is converted to the pathogenic form through a prion-like mechanism. Pathogenic Aβ causes levels of reactive oxygen species (ROS) and endothelin-1 (ET-1) to increase, the latter acting on ET_A receptors on pericytes, causing contraction and capillary constriction. The resulting decrease in CBF promotes Aβ production and inhibits its clearance. (b) Schematic of a brain capillary network, lined with pericytes (cf. [31, fig. 2]).

These models often exhibit prion-like behaviour by assuming, *a priori*, that the disease-free state is inherently unstable, even to minute seeds of pathogenic proteins, therefore ensuring that any seeding event leads inevitably to accumulation and propagation. A prominent example is Prusiner's heterodimer model, initially proposed for the major prion protein (PrP) [52] and frequently employed to model Aβ kinetics [47,49,53]. In such models, disease outbreak is typically triggered by introducing a small pathogenic protein seed at some spatial location, though the origin of this initial seed is not usually addressed.

The role of brain vasculature in AD has received less attention from mathematical modellers compared with the prion-like characteristics of the disease. To our knowledge, the two have not been combined in any single model; the closest example might be Craft *et al.* [43], who treat plasma as a homogeneous compartment into which Aβ is cleared. Sophisticated biophysical models of image-derived brain capillary networks have been used to estimate the decrease in CBF caused by Aβ-induced capillary occlusions [32], as well as to study the emergence of critical tissue regions where Aβ clearance might be impaired due to reduced flow rates [54]. However, these studies do not account for the prion-like kinetics of Aβ, nor do they account for the two-way coupling of Aβ and capillary health.

Outline and approach. The goal of this paper is to bridge the gap between the prion-like nature of Aβ on the one hand and Aβ-microvascular interaction on the other. We construct a mathematical model that integrates (i) the prion-like kinetics of Aβ, (ii) Aβ-induced capillary constriction, and (iii) the effects of decreased CBF on Aβ production and clearance rates. In so doing, we formalize the long-standing positive feedback loop hypothesis cited above (see [14,17,30] and figure 1), and uncover the implications of its integration with the prion-like hypothesis of AD [4–9], especially for disease initiation and spatial propagation.

Our primary result in this regard is the emergence of bistability in the dynamics of Aβ-microvascular pathology, wherein it is possible for the disease-free state to be metastable, i.e. stable only to sufficiently small pathogenic seeds (§3). We investigate the consequences of this bistability for the spatio-temporal disease dynamics in the human connectome network (figure 5), uncovering several threshold phenomena relevant to disease initiation and spread (§4). Finally, we demonstrate mathematically how a focal deficit in arterial blood supply to a region of brain tissue can be sufficient, in the context of the mechanisms summarized in figure 1, to trigger prion-like disease outbreak, *without* introducing a seed of pathogenic Aβ (figure 10), consistent with the two-hit vascular hypothesis of AD (§5).

The model of Aβ–CBF interaction in a small region of the brain is constructed in §2, and as far as is practicable, we aim to derive it from mechanistic biological principles, most of which

are depicted in figure 1. Readers who wish to understand the dynamics of the model without the details of its construction can skip to §2c. In analysing the model's behaviour, we focus on its qualitative properties, particularly the asymptotic behaviour of solutions (representing disease prognosis) and the bifurcations (threshold phenomena) that illuminate the boundaries between distinct asymptotic behaviours (for a primer on bifurcations, see appendix E in the electronic supplementary material). Once we have analysed the dynamics of the single-region model in §3, we proceed to analyse the spatio-temporal model on the connectome network (comprising many brain regions connected by neuronal pathways) in §§4 and 5.

2. Model derivation for a single region

(a) The heterodimer model

For the protein kinetics of Aβ, we adopt Prusiner's heterodimer model [52], possibly the simplest mechanistic model of prion-like behaviour. It describes the evolution of two concentrations over time: that of the *normal form* of Aβ, P, and that of its *pathogenic form*, $\tilde{P}$. The normal form is produced endogenously from the amyloid precursor protein (APP) and is non-toxic. The pathogenic form has a misfolded structure, which it can impart to normal Aβ proteins with which it comes into contact (see figure 1a). This interaction gives rise to an autocatalytic process, akin to an infectious disease, and is summarized by the chemical reaction $P + \tilde{P} \to 2\tilde{P}$.

Rate equations. The rate equations of the heterodimer model are

$$\frac{\mathrm{d}p}{\mathrm{d}t} = \mu - \lambda p - kp\tilde{p} - mp \tag{2.1a}$$

and

$$\frac{\mathrm{d}\tilde{p}}{\mathrm{d}t} = kp\tilde{p} - \tilde{\lambda}\tilde{p} + mp, \tag{2.1b}$$

where p and $\tilde{p}$ denote the concentrations of P and $\tilde{P}$, respectively, μ is the production rate of P; λ and $\tilde{\lambda}$ are the clearance rates of P and $\tilde{P}$, respectively (via the vascular and glymphatic systems, for example); k is the catalytic conversion rate of P to $\tilde{P}$; and m is the rate of spontaneous conversion (also known as non-catalytic conversion).

Because spontaneous conversion is thought to be rare and sporadic [8], i.e. $m \ll 1$, it is often disregarded by modellers [47,55–57], i.e. $m = 0$. However, if m is small but positive, we will see that equation (2.1) exhibits dynamics that are subtly different to the $m = 0$ case. In order to understand these differences, we assume throughout that $0 \leq m \ll 1$.

The basic reproduction number. In Prusiner's heterodimer model, μ, λ, $\tilde{\lambda}$, k and m are constants, and similar to models of infectious diseases, the character of the dynamics is largely determined by a dimensionless combination of these constants, namely the *basic reproduction number*:

$$R_0 = \frac{\mu k}{\lambda\tilde{\lambda}}. \tag{2.2}$$

For $R_0 < 1 - O(m)$, there is a stable *healthy equilibrium* at which $p = \mu/\lambda - O(m)$ and $\tilde{p} = O(m)$. As R_0 increases through unity, a stable *diseased equilibrium* appears, at which $p = \tilde{\lambda}/k - O(m)$ and $\tilde{p} = \mu/\tilde{\lambda} - \lambda/k + O(m)$. If $m = 0$, the diseased equilibrium bifurcates through the healthy equilibrium transcritically (marked 'TC' in figure 2). For positive but small m, however, an *imperfection* [58, §2.3] is introduced: the diseased and healthy equilibria now belong to the same branch, which moves away from the $\tilde{p} = 0$ axis without bifurcation as R_0 increases through unity; see figure 2. In short, the $\tilde{p} = 0$ branch of equilibria is destroyed by this perturbation in m, revealing the structural instability of the $m = 0$ case.

When the heterodimer model is employed to produce disease-like behaviour, e.g. [46–49,55,56,59], R_0 must be chosen greater than unity, for otherwise, the healthy equilibrium

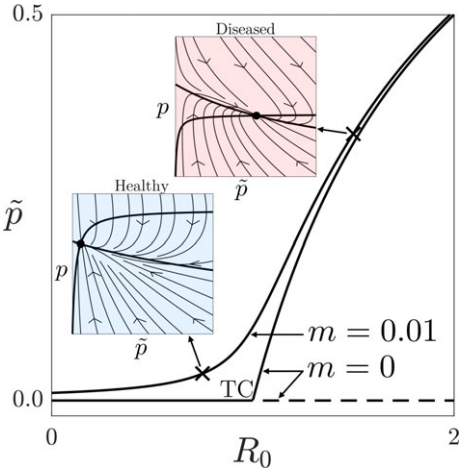

Figure 2. Bifurcation diagram for Prusiner's heterodimer model (2.1). Stable and unstable branches of equilibria are solid and dashed, respectively (only non-negative branches are shown). 'TC' marks a transcritical bifurcation point. Insets: Phase portraits of healthy (blue) and diseased (red) dynamics at $R_0 = 0.75$ and $R_0 = 1.5$, respectively, showing the unique positive equilibrium at the intersection of the system's nullclines.

is a global attractor, implying the *impossibility* of disease outbreak. If $R_0 > 1$, however, then the diseased equilibrium is a global attractor, implying the *inevitability* of disease outbreak [60,61].

It may be that $R_0 > 1$ in some individuals, e.g. due to enhanced Aβ production in familial AD caused by mutations in the APP and/or presenilin genes [62], or age-related decreases in Aβ clearance [63,64]. Our focus here, however, is to study the possible effects of vascular damage on Aβ dynamics, absent any other predisposition to disease such as the above. Therefore, we will assume that $R_0 < 1$ throughout.

The remainder of this section concerns the extension of equation (2.1) to incorporate vascular effects: first, the influence of CBF on Aβ production and clearance rates, and second, the vasoconstrictive and ischaemic effects of Aβ.

Sensitivity of production and clearance to hypoperfusion. When CBF falls, the production rate of Aβ increases and its clearance rate decreases (figure 1a). We assume for simplicity that these relationships are linear:

$$\mu = \mu_0 + \beta(1-q), \quad \lambda = \lambda_0 - \gamma(1-q) \quad \text{and} \quad \tilde{\lambda} = \tilde{\lambda}_0 - \tilde{\gamma}(1-q), \tag{2.3}$$

where q is the normalized CBF rate (to be defined precisely later), with $q = 1$ and $q = 0$ corresponding to normal CBF and a total collapse in CBF, respectively. In healthy conditions, $q = 1$ and Aβ is produced and cleared at the *base rates* μ_0, λ_0 and $\tilde{\lambda}_0$. We call β, γ and $\tilde{\gamma}$ the (*hypoperfusion-*)*sensitivity parameters*. Prusiner's heterodimer model (2.1) corresponds to $\beta = \gamma = \tilde{\gamma} = 0$. By substituting equation (2.3) into equation (2.2), we see that R_0 increases in response to decreases in q. Next, we turn to the influence of pathogenic Aβ on q.

(b) Capillary networks and cerebral blood flow

As depicted in figure 1a, (i) pathogenic Aβ causes capillary constrictions, (ii) CBF falls as a result of capillary constrictions, and (iii) hypoperfusion influences the protein kinetics of Aβ. We have just modelled (iii) with equation (2.3). Below, we model (i) and (ii). First, we will derive a formula for the 'open capillary fraction' κ in terms of $\tilde{p}$; this is equation (2.7). Then we will use numerical simulations to relate κ to the normalized CBF rate q in a simple random graph model of a brain

capillary network. The eventual result of this subsection will then be a formula for q in terms of $\tilde{p}$ (equation (2.15)), thus closing the Aβ–CBF feedback loop opened by equation (2.3).

(i) Capillary constrictions due to Aβ

Pericytes contract when exposed to Aβ oligomers [14] (see §1 and figure 1). Aβ oligomers, but not monomers, cause reactive oxygen species (ROS) to be generated in pericytes and/or endothelia, and these ROS trigger the release of the vasoconstrictor peptide ET-1 [14].

We model these relationships as the first-order chemical reactions

$$\varnothing \underset{a_2}{\overset{a_1\tilde{p}}{\rightleftarrows}} \mathrm{ROS} \quad \text{and} \quad \varnothing \underset{a_4}{\overset{a_3[\mathrm{ROS}]}{\rightleftarrows}} \text{ET-1}, \tag{2.4}$$

where $\varnothing$ represents chemical species external to the model [65], $\tilde{p}$ denotes the concentration of pathogenic Aβ, [ROS] denotes the concentration of ROS, and the a_i parameters are rate constants.

Pericyte contraction is triggered by the binding of ET-1 to ET_A receptors on pericytes, and can be reversed by removing the Aβ oligomers [14]. Thus, we model the state of each pericyte as a reversible reaction:

$$\text{relaxed} \underset{a_6}{\overset{a_5[\text{ET-1}]}{\rightleftarrows}} \text{contracted}. \tag{2.5}$$

Because pericyte contraction occurs within minutes of Aβ exposure [14], whereas the half-life of Aβ in vivo is approximately 8 h [66], we treat reactions (2.4) and (2.5) as quasi-static, so that the probability of a given pericyte's being relaxed is found to be

$$\mathbb{P}(\text{relaxed}) = (1 + c\tilde{p})^{-1}, \tag{2.6}$$

where we define the *contraction ratio* $c := a_1a_3a_5/a_2a_4a_6$.

We define the *open capillary fraction* κ as the mean fraction of capillaries that either do not host a pericyte or host a pericyte that is relaxed. Denoting by $\phi \in (0, 1]$ the fraction of capillaries that host a pericyte, we obtain

$$\kappa = 1 - \phi + \phi \cdot \mathbb{P}(\text{relaxed}) = \frac{1 + c(1-\phi)\tilde{p}}{1 + c\tilde{p}}. \tag{2.7}$$

Therefore, κ is a decreasing function of $\tilde{p}$: the higher the pathogenic Aβ concentration, the lower the (mean) open capillary fraction.

(ii) Hypoperfusion due to capillary constrictions

When capillaries are constricted ($\kappa < 1$), microvascular resistance increases, leading to hypoperfusion ($q < 1$). But what is the nature of the CBF decrease in response to progressive constrictions? For example, does q change suddenly near a critical κ, or is the decrease gradual? Below, we pursue a mechanistic understanding of the κ–q relationship, first by constructing a simple network model of the capillary bed and its conduction of blood, followed by a numerical study of how the network's hydraulic conductance (inverse of resistance) depends on the conductances of its individual edges (capillaries).

Capillary networks and cerebral blood flow. We model the brain microvasculature as a collection of network units, each fed by a single penetrating arteriole and drained by a single ascending venule (figure 1b). Edges are capillaries and vertices are their junctions. Most vertices in brain capillary networks have degree three [67]. Therefore, we follow Goirand *et al.* [68] in modelling our capillary network units as degree-three random regular graphs (RRGs), the simplest model of a degree-three network [69] (figure 3a).

We assume that all capillaries have the same conductance, which we scale to unity, thereby neglecting the heterogeneity of vessel diameters and lengths. We also neglect the complex rheological properties of blood in the microcirculation, e.g. the Fåhræus, Fåhræus–Lindqvist, and phase separation effects [70]. Instead, we assume only that the flow rate into a vertex equals the

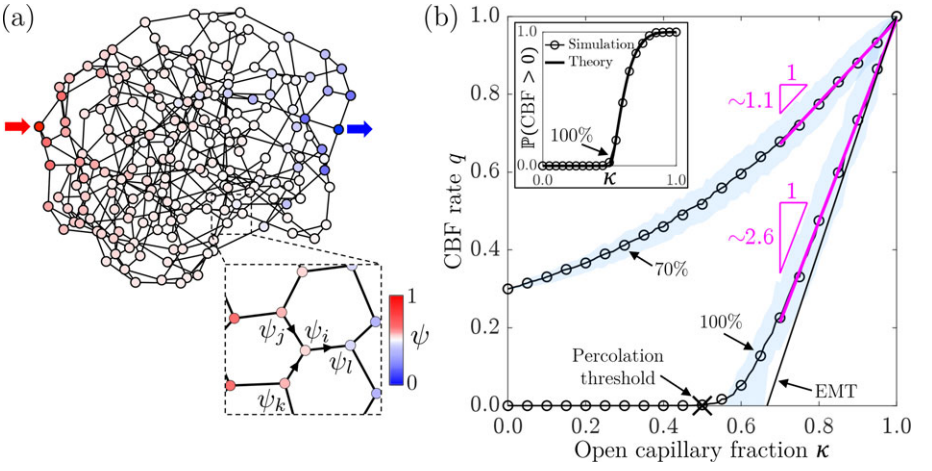

Figure 3. Hypoperfusion due to capillary constrictions. (a) An RRG with $n + 2 = 300$ vertices; ψ is (normalized) pressure. (b) Numerical study of the q–κ relationship; solid lines with circles denote normalized flow rate sample mean q with respect to the open capillary fraction κ over 1000 numerical simulations on an RRG with $n + 2 = 1000$ vertices, for 100% and 70% conductance decrease in constricted capillaries. Envelopes are interquartile ranges. Pink lines are lines of best fit on the interval $\kappa \in [0.7, 1]$. 'EMT' indicates effective medium theory prediction (see main text). Inset: probability of non-zero CBF rate with respect to open capillary fraction κ; solid lines with circles indicate sample mean over 1000 numerical simulations, dark solid line indicates formula (2.12).

flow rate out of it (Kirchhoff's Law), and that the flow rate through a capillary is proportional to the pressure drop across its two vertices (Ohm's Law), a common approximation [68,71]. Later, we will compare our results with those of more physiologically accurate models in the literature [32,54], and will find that these simplifications do not have a marked effect on the κ–q relationship.

We choose the *inlet* and *outlet* vertices, representing the interface between the network and the arteriole–venule pair, uniformly at random from the vertex set $V = \{1, 2, \ldots, n + 2\}$, and label the inlet by $n + 1$ and the outlet by $n + 2$ without loss of generality.

Blood is driven through the network by the pressure difference Ψ between the inlet and outlet. Denoting by ψ_i the fluid pressure at vertex i, we fix $\psi_{n+1} = 1$ and $\psi_{n+2} = 0$, thereby prescribing a unit pressure drop across the network, i.e. $\Psi = 1$ (figure 3a).

Kirchhoff's and Ohm's Laws give rise to a linear algebraic system to be solved for the pressure vector $\boldsymbol{\psi} = (\psi_1, \psi_2, \ldots, \psi_n)^\top$. Denoting by $\mathcal{N}_{\text{inlet}}$ and $\mathcal{N}_{\text{outlet}}$ the sets of vertices neighbouring the inlet and outlet, and by $\{\mathbf{e}_i\}$ the standard basis of $\mathbb{R}^n$, we obtain

$$\Lambda\boldsymbol{\psi} = \sum_{i \in \mathcal{N}_{\text{inlet}}} (1 - \psi_i)\mathbf{e}_i - \sum_{j \in \mathcal{N}_{\text{outlet}}} \psi_j \mathbf{e}_j, \tag{2.8}$$

where Λ is the $n \times n$ Laplacian matrix of the capillary network (excluding the inlet and outlet),

$$\Lambda = (\Lambda_{ij}) \quad \text{and} \quad \Lambda_{ij} = \delta_{ij} \sum_{k=1}^{n} a_{ik} - a_{ij}, \tag{2.9}$$

where a_{ij} is 1 if ij is in the edge set and 0 otherwise, and δ_{ij} is the Kronecker delta. Solving equation (2.8) for $\boldsymbol{\psi}$, we obtain the total flow rate through the network

$$Q_0 = \sum_{i \in \mathcal{N}_{\text{inlet}}} (1 - \psi_i), \tag{2.10}$$

which we call the healthy CBF rate.

Cerebral blood flow following constrictions. When edges are constricted, their corresponding edge conductances a_{ij} decrease from 1 to some $\bar{a} \in [0, 1)$, thereby changing certain entries in the Laplacian matrix (2.9) and the solution $\boldsymbol{\psi}$ of equation (2.8). The decrease in a_{ij} following pericyte contraction has been estimated at 70% by Nortley *et al.*, though they note this is likely an underestimate since it assumes Poisseuille flow, neglecting blood's higher effective viscosity at the capillary scale [14]. It also neglects the liability of large blood cells like neutrophils to occlude the constricted lumen altogether [30,32], modelled as a near-100% decrease in capillary conductance by Cruz Hernández *et al.* [32]. Thus, we assume that the conductance of a constricted capillary is 70–100% lower than that of an open capillary, that is, $\bar{a} \in [0, 0.3]$.

Re-computing equation (2.10) after constrictions yields a CBF rate $Q < Q_0$. We define the *normalized CBF rate* as

$$q = \frac{Q}{Q_0}, \tag{2.11}$$

and turn next to its dependence on the open capillary fraction κ.

Percolation and conduction. Given an open capillary fraction $\kappa \in [0, 1]$, we assume that the constricted capillaries are distributed uniformly at random throughout the network.

For $\bar{a} = 0$, i.e. 100% decrease in edge conductance, and assuming n is large, we can estimate analytically the critical value κ_c below which the expected CBF rate is zero, i.e. the *percolation threshold* of the network. A standard computation [72, §15] yields

$$\mathbb{P}(q > 0 \mid \kappa) = \left(\left[1 - \left(\kappa^{-1} - 1 \right)^3 \right]_+ \right)^2, \tag{2.12}$$

where $[X]_+$ denotes $\max\{X, 0\}$ (see figure 3b, inset), whence

$$\kappa_c = \inf\{\kappa : \mathbb{P}(q > 0 \mid \kappa) > 0\} = 1/2. \tag{2.13}$$

To estimate $\mathbb{E}(q \mid \kappa)$ for $\kappa > \kappa_c = 1/2$, we resort to numerical simulations. Having generated an RRG network with $n + 2 = 1000$ vertices, we replaced $a_{ij} = 1$ with $\bar{a} = 0$ in a randomly selected proportion κ of edges, solved equation (2.8), and computed q. We repeated this procedure 1000 times for each κ in a range of values between 0 and 1. The resulting sample mean $\mathbb{E}(q \mid \kappa)$ is shown in figure 3b.

Upon visual inspection, the dependence of q on κ is roughly linear for $\kappa > 0.7$, and a linear regression yields a line of best fit with slope ∼2.6, consistent with previous computational studies of anatomically accurate brain capillary networks.[1] This slope is also close to the prediction of 3.0 given by the effective medium theory of Kirkpatrick [74,75] (labelled 'EMT' in figure 3b), a semi-analytic method for predicting the q–κ relationship in lattice networks with uniform degree.

We repeated the simulations above, this time for a 70% decrease in the conductance of constricted capillaries, i.e. $\bar{a} = 0.3$. As before, there are no sharp changes in q as κ is varied, and the line of best fit for $\kappa > 0.7$ has slope ∼1.1.

Based on these computational findings, we treat q henceforth as a linear function of κ with slope α in the approximate range of 1.2–2.6:

$$q = \alpha(\kappa - 1) + 1. \tag{2.14}$$

Note that, by definition, $q = 1$ when $\kappa = 1$. We ignore the nonlinear portion of the q–κ relationship, below $\kappa \approx 0.6$, since we do not expect capillary constrictions to exceed 40%; specifically, we assume $\phi \leq 1/\alpha$, which, together with equation (2.7), guarantees formula (2.14) remains positive.

[1]Cruz Hernández *et al.* [32] analysed large, anatomically accurate microvascular networks (10 000 vessels) from the cortex of mice and humans, and obtained a range of slopes between 2.1 and 2.9. Goirand [73], also studying anatomically accurate networks but this time with uniform vessel conductances, found a slope of 2.75.

royalsocietypublishing.org/journal/rspa Proc. R. Soc. A 481: 20240548

Table 1. Dimensionless model parameters.

parameter	meaning	base value
R_0	basic reproduction number	0.75
ϵ	toxic to normal clearance rate ratio	1
m	spontaneous misfolding rate	0.001
c	contraction ratio	10
β	hypoperfusion-sensitivity of Aβ production rate	0.3
γ	hypoperfusion-sensitivity of normal Aβ clearance rate	0.2
$\tilde{\gamma}$	hypoperfusion-sensitivity of pathogenic Aβ clearance rate	0.2

Finally, substituting the κ–$\tilde{p}$ relationship (2.7) into equation (2.14), we obtain a formula for the mean normalized CBF rate q as a function of $\tilde{p}$,

$$q(\tilde{p}) = 1 - \alpha\phi\frac{\tilde{p}}{c^{-1}+\tilde{p}}, \tag{2.15}$$

thus closing the model of Aβ–CBF interaction in a single region of the connectome.

(c) The model for a single region

Substituting equation (2.15) into equations (2.3) and (2.1), we obtain a modified form of the heterodimer model:

$$\frac{\mathrm{d}p}{\mathrm{d}t} = \mu(\tilde{p}) - \lambda(\tilde{p})p - kp\tilde{p} - mp \tag{2.16a}$$

and

$$\frac{\mathrm{d}\tilde{p}}{\mathrm{d}t} = kp\tilde{p} - \tilde{\lambda}(\tilde{p})\tilde{p} + mp, \tag{2.16b}$$

where

$$\left.\begin{aligned} &\mu(\tilde{p}) = \mu_0 + \beta\alpha\phi\frac{\tilde{p}}{c^{-1}+\tilde{p}}, \quad \lambda(\tilde{p}) = \lambda_0 - \gamma\alpha\phi\frac{\tilde{p}}{c^{-1}+\tilde{p}} \\ \text{and} \quad &\tilde{\lambda}(\tilde{p}) = \tilde{\lambda}_0 - \tilde{\gamma}\alpha\phi\frac{\tilde{p}}{c^{-1}+\tilde{p}}. \end{aligned}\right\} \tag{2.17}$$

We non-dimensionalize the model by introducing the following scalings:

$$p = \frac{\mu_0}{\lambda_0}\hat{p}, \quad \tilde{p} = \frac{\mu_0}{\tilde{\lambda}_0}\hat{\tilde{p}} \quad \text{and} \quad t = \frac{1}{\tilde{\lambda}_0}\hat{t}, \tag{2.18}$$

where circumflexes indicate dimensionless quantities. The following dimensionless parameters, which are also listed in table 1, arise upon substitution of equation (2.18) into equation (2.16):

$$\left.\begin{aligned} &R_0 = \frac{k\mu_0}{\lambda_0\tilde{\lambda}_0}, \quad \epsilon = \frac{\tilde{\lambda}_0}{\lambda_0}, \quad \hat{m} = \frac{m}{\lambda_0} \\ &\hat{c} = \frac{\mu_0 c}{\tilde{\lambda}_0}, \quad \hat{\beta} = \frac{\beta\alpha\phi}{\mu_0}, \quad \hat{\gamma} = \frac{\gamma\alpha\phi}{\lambda_0} \quad \text{and} \quad \hat{\tilde{\gamma}} = \frac{\tilde{\gamma}\alpha\phi}{\tilde{\lambda}_0}. \end{aligned}\right\} \tag{2.19}$$

We also introduce the dimensionless production and clearance rate functions:

$$\hat{\mu}(\hat{\tilde{p}}) = \frac{\mu(\tilde{p})}{\mu_0}, \quad \hat{\lambda}(\hat{\tilde{p}}) = \frac{\lambda(\tilde{p})}{\lambda_0}, \quad \hat{\tilde{\lambda}}(\hat{\tilde{p}}) = \frac{\tilde{\lambda}(\tilde{p})}{\tilde{\lambda}_0}. \tag{2.20}$$

Dropping circumflexes henceforth, the dimensionless model is

$$\epsilon\frac{\mathrm{d}p}{\mathrm{d}t} = \mu(\tilde{p}) - \lambda(\tilde{p})p - R_0p\tilde{p} - mp \tag{2.21a}$$

and

$$\frac{\mathrm{d}\tilde{p}}{\mathrm{d}t} = R_0 p\tilde{p} - \tilde{\lambda}(\tilde{p})\tilde{p} + mp, \tag{2.21b}$$

where

$$\mu(\tilde{p}) = 1 + \beta\frac{\tilde{p}}{c^{-1}+\tilde{p}}, \quad \lambda(\tilde{p}) = 1 - \gamma\frac{\tilde{p}}{c^{-1}+\tilde{p}} \quad \text{and} \quad \tilde{\lambda}(\tilde{p}) = 1 - \tilde{\gamma}\frac{\tilde{p}}{c^{-1}+\tilde{p}}. \tag{2.22}$$

Model summary. The dimensionless planar system equation (2.21) is our model of Aβ-CBF dynamics in a single region of the connectome. We obtained it by assuming: (a) that Aβ is a prion-like protein with normal and pathogenic forms, and that its production and clearance rates depend on the CBF rate; (b) that pathogenic Aβ tends to constrict capillaries, causing the open capillary fraction κ to decrease; and (c) that the CBF rate decreases linearly as κ decreases, informed by numerical simulations on a random graph model of a capillary network. Recall that κ and q do not appear explicitly in equation (2.21) because the time scales on which they adjust to the pathongenic Aβ concentration $\tilde{p}$ are very short, so that they are in quasi-equilibrium with $\tilde{p}$.

The model has seven dimensionless parameters (table 1), three of which (R_0, ϵ, m) appear already in our version (2.1) of Prusiner's heterodimer model; recall $0 \le m \ll 1$. The other four (c, β, γ, $\tilde{\gamma}$) modulate the coupling strength between Aβ and the microvasculature; it will transpire that these four parameters have similar influences over the model's behaviour.

In the coming sections, we analyse the dynamics of equation (2.21) in depth (§3), followed by its spatially extended counterpart on the connectome network (§§4 and 5).

3. Disease dynamics in a single region

In this section, we study the dynamics of system (2.21). Recall that p and $\tilde{p}$ denote the dimensionless concentrations of normal and pathogenic Aβ in a single region of interest (ROI) of the connectome.

(a) Bistability and threshold effect

The basic reproduction number R_0 continues to play a crucial role, as it did for Prusiner's heterodimer model (§2a). A linear analysis of equation (2.21) reveals that when $R_0 < 1 - O(m)$, there is a stable *healthy equilibrium* $(p^h, \tilde{p}^h) \approx (1, 0)$, and when $R_0 > 1$, there is a stable *diseased equilibrium* $(p^d, \tilde{p}^d)$ with $\tilde{p}^d = O(1)$. Unlike Prusiner's heterodimer model, however, stable healthy and diseased equilibria may coexist when $R_0 < 1$ provided the Aβ–CBF coupling is sufficiently strong, as we now show.

Phase plane. Equilibria lie at the intersections of the nullclines shown in figure 4a, given by

$$\frac{\mathrm{d}p}{\mathrm{d}t} = 0 \iff p = \nu(\tilde{p}) := \frac{\mu(\tilde{p})}{\lambda(\tilde{p}) + R_0\tilde{p} + m} \tag{3.1a}$$

and

$$\frac{\mathrm{d}\tilde{p}}{\mathrm{d}t} = 0 \iff p = \tilde{\nu}(\tilde{p}) := \frac{\tilde{\lambda}(\tilde{p})\tilde{p}}{R_0\tilde{p} + m}. \tag{3.1b}$$

When Aβ–CBF coupling is absent, i.e. Prusiner's original heterodimer model (2.1), $\mu(\tilde{p})$, $\lambda(\tilde{p})$ and $\tilde{\lambda}(\tilde{p})$ all equal 1 (recall (2.22)). In this case, the nullclines $p = \nu(\tilde{p})$ and $p = \tilde{\nu}(\tilde{p})$ are shown in figure 2. In particular, for $R_0 < 1$, they intersect only at the healthy equilibrium $(p^h, \tilde{p}^h) \approx (1, 0)$.

When one or more of c, β, γ, $\tilde{\gamma}$ is increased, the nullclines are deformed continuously in the phase plane: the graph of $p = \nu(\tilde{p})$ rises and that of $p = \tilde{\nu}(\tilde{p})$ falls. For fixed $R_0 < 1$, if c, β, γ, $\tilde{\gamma}$ are made sufficiently large, then the phase plane in figure 2 is deformed to the phase plane in figure 4a. Indeed, a saddle-node (SN) bifurcation occurs at the nullclines' tangential intersection, whence two new positive equilibria are born. A linear analysis confirms that one is a saddle and

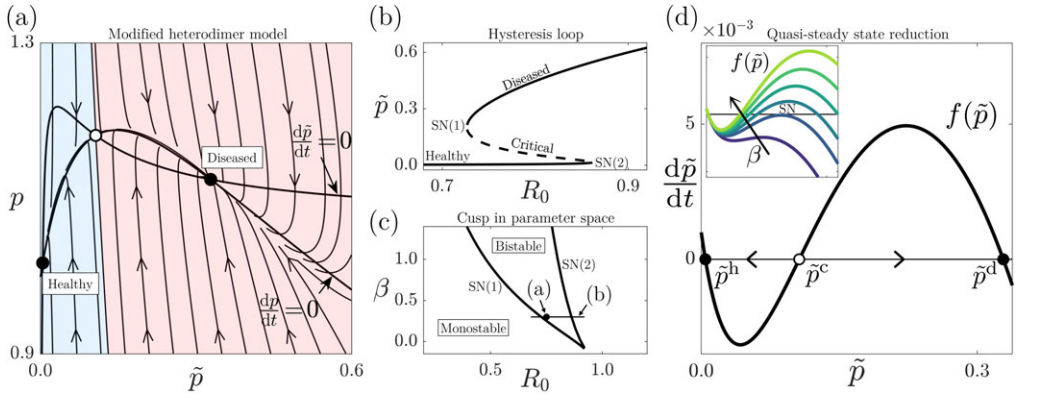

Figure 4. Bistable dynamics emerging from Aβ-capillary coupling. (a) Phase portrait of system (2.21) with parameter values as given in table 1. Nullclines (3.1) shown in black; stable and unstable equilibria shown as black and white circles, respectively; healthy and diseased domains of attraction highlighted in blue and red, respectively. (b) Bifurcation diagram showing the $\tilde{p}$-coordinate of the system's equilibria as R_0 is varied; stable and unstable branches are solid and dashed, respectively; 'SN(1)' and 'SN(2)' indicate saddle-node bifurcations. (c) Cusp separating the mono- and bistable regimes in a R_0-β slice of parameter space (other parameters as in table 1); the parameter values corresponding to panels (a,b) are indicated by a point and line segment, respectively. (d) One-dimensional dynamics of equation (3.2), obtained from the quasi-steady-state approximation, for $\epsilon \lesssim 1$, of the planar dynamics. Inset: the function f for values of β between 0.2 (purple) and 0.35 (light green).

the other is a stable node, which we denote by $(p^c, \tilde{p}^c)$ and $(p^d, \tilde{p}^d)$, respectively ('c' for 'critical' and 'd' for 'diseased').

This bistability emerges from the biological assumptions outlined in §1 and figure 1. The key insight is that stable healthy and diseased equilibria, $(p^h, \tilde{p}^h)$ and $(p^d, \tilde{p}^d)$, can coexist when $R_0 < 1$ provided the kinetics of Aβ are sufficiently sensitive to hypoperfusion (β, γ, $\tilde{\gamma}$ large enough) and capillaries are sufficiently sensitive to pathogenic Aβ (c large enough).

Critical seed size. An important implication of bistability is a new threshold phenomenon: the healthy equilibrium remains stable but is no longer globally stable. The healthy (blue) and diseased (red) domains of attraction are shown in figure 4a; their separatrix is the stable manifold of $(p^c, \tilde{p}^c)$. For $\epsilon \lesssim 1$, we see from figure 4a that, near the healthy equilibrium, the separatrix is roughly parallel to the p-axis. Therefore, the *critical seed size*, i.e. the minimum $\tilde{p}$ such that $(p^h, \tilde{p})$ is not in the healthy domain of attraction, is roughly $\tilde{p}^c$ when $\epsilon \lesssim 1$.

Hysteresis and hard loss of stability. By increasing some or all of c, β, etc., the bifurcation diagram of Prusiner's heterodimer model in figure 2 is deformed into the 'S-shaped' bifurcation diagram in figure 4b which is characteristic of hysteresis.

As R_0 increases, the healthy equilibrium now undergoes a *hard loss of stability* at $R_0 = 1 - O(m)$, via transcritical bifurcation if $m = 0$, or a saddle-node bifurcation if $m > 0$ (marked 'SN(2)' in figure 4b). In order to return to the healthy state, however, it is not enough to decrease R_0 back below unity; rather, a lower threshold exists below which R_0 must fall for the diseased equilibrium to be eliminated (marked 'SN(1)' in figure 4b).

(b) Quasi-steady-state reduction

Before introducing spatial variation in §4, we reduce the regional model from the planar system (2.21) to a scalar equation by exploiting its fast-slow form, thereby greatly simplifying later analyses.

We expect the clearance rate of pathogenic Aβ to be less than that of normal Aβ, i.e. $\epsilon = \tilde{\lambda}_0/\lambda_0 < 1$. The ϵ parameter can also be understood as a ratio of characteristic time scales, i.e. $\epsilon = (1/\lambda_0)/(1/\tilde{\lambda}_0)$: if ϵ is small, then the dynamics of p is fast relative to that of $\tilde{p}$. Even for $\epsilon = 1$, the phase plane figure 4a exhibits near-vertical orbits, i.e. $|\mathrm{d}p/\mathrm{d}t| \gg |\mathrm{d}\tilde{p}/\mathrm{d}t|$. In this case, the quasi-steady-state approximation (QSSA) applies [76, §8.3]: after a short transient, p achieves quasi-steady-state in a neighbourhood of the $p = \nu(\tilde{p})$ nullcline. Substituting $\nu(\tilde{p})$ for p in equation (2.21), we then obtain a scalar equation that governs the slow (relative to p) dynamics of $\tilde{p}$:

$$\frac{\mathrm{d}\tilde{p}}{\mathrm{d}t} = f(\tilde{p}) := (R_0\tilde{p} + m)\nu(\tilde{p}) - \tilde{\lambda}(\tilde{p})\tilde{p}. \tag{3.2}$$

We call $f(\tilde{p})$ the *reaction function*. In the bistable parameter regime, a slice of which is shown in figure 4c, $f(\tilde{p})$ has three roots, namely $\tilde{p}^h$ (stable), $\tilde{p}^c$ (unstable) and $\tilde{p}^d$ (stable), as illustrated in figure 4d.

The QSSA remains valid outside the bistable parameter regime, too. Take for example Prusiner's heterodimer model ($c = \beta = \gamma = \tilde{\gamma} = 0$) with $R_0 > 1$ and $m = 0$, a popular model of prion-like dynamics [46–49,55,56]. In this case,

$$\frac{\mathrm{d}\tilde{p}}{\mathrm{d}t} = f(\tilde{p}) = \tilde{p}\left(1 - \frac{R_0}{R_0 - 1}\tilde{p}\right)\frac{R_0 - 1}{1 + R_0\tilde{p}}, \tag{3.3}$$

which produces equivalent dynamics to the logistic equation (obtained by replacing $1 + R_0\tilde{p}$ in the denominator of the final term with 1).

For the remainder of the paper, we assume that ϵ is sufficiently small and adopt the scalar reduction (3.2) of the regional model (2.21). For a fuller discussion of the QSSA, in particular its inapplicability to the case of $\epsilon \gg 1$ (equivalently $\tilde{\lambda}_0 \gg \lambda_0$), see appendix B in the electronic supplementary material.

4. Network disease dynamics

Modelling axonal transport. Aβ spreads along axonal fibre tracts between neuronally connected brain regions, moving in both anterograde and retrograde directions [77,78]. Though the precise transport mechanisms are not fully understood, it is common to model the spatial spread of Aβ as a diffusion process through the structural connectome network [79–81].

The nodes of the connectome are 'regions of interest' (ROIs) obtained from a parcellation scheme [82]; we will use the 83-node Lausanne parcellation [83] (see figure 5) to illustrate the analyses of the present and next sections. The edges, representing axonal connections, derive from magnetic resonance diffusion tractography, which estimates the number of fibres n_{ij} connecting each pair of regions ij in the parcellation [83]. The result is an N-dimensional ($N = 83$) dynamical system governing the pathogenic Aβ concentration at each ROI:

$$\frac{\mathrm{d}\tilde{p}_i}{\mathrm{d}t} = D\sum_{j=1}^{N} w_{ij}(\tilde{p}_j - \tilde{p}_i) + f(\tilde{p}_i), \quad i = 1, \ldots, N, \tag{4.1}$$

where D is a diffusion coefficient, w_{ij} is the ij edge weight, and f is the reaction function (3.2). We let $w_{ij} = w_{ji} = n_{ij}/l_{ij}^2$, where n_{ij} is the number of fibres connecting i and j, and l_{ij} is their length; see [85] for a discussion of this and other choices of $w_{ij} = w_{ij}(n_{ij}, l_{ij})$.

Model behaviour. Several prion-like modelling studies have treated equation (4.1) when $m = 0$ and $\tilde{p}^h = 0$ is an *unstable* root of $f(\tilde{p})$ [47,49,55,86], in which case the dynamics are simple and well-understood, namely:

$$\text{if } R_0 > 1, \text{ then either } \tilde{p}_i \equiv 0 \text{ for all } i \text{ or } \tilde{p}_i \to \tilde{p}^d \text{ as } t \to \infty \quad \text{for all } i.$$

That is, the brain-wide diseased state $(\tilde{p}_1, \ldots, \tilde{p}_N) = (\tilde{p}^d, \ldots, \tilde{p}^d)$ attracts *all* states except for the brain-wide healthy state $(\tilde{p}_1, \ldots, \tilde{p}_N) = (0, \ldots, 0)$. Therefore, arbitrarily small pathogenic seeds,

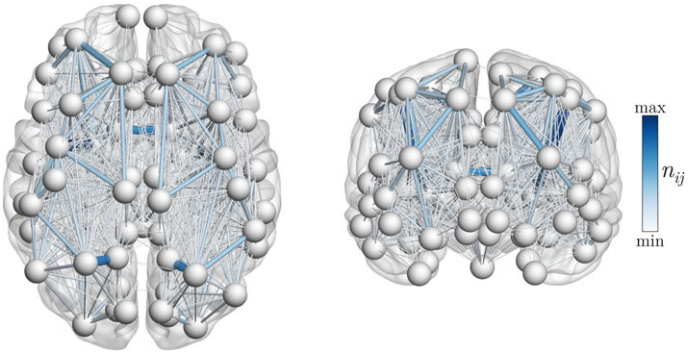

Figure 5. Axial and coronal views of the connectome network (83-node Lausanne parcellation [83]), with darker, thicker edges indicating larger fibre number n_{ij}. For the GraphML file and processing details, see the electronic supplementary material. All connectome visualizations in the paper were created with BrainNet [84].

placed anywhere in the connectome, *guarantee* outbreak and spatial propagation of disease. (This fact follows from the comparison principle stated below.)

The goal of this section is to gain insight into equation (4.1) when $f(\tilde{p})$ is *bistable*, i.e. takes the form shown in figure 4d. That is, we assume that $R_0 < 1$ and that the Aβ–CBF coupling (i.e. c, β, γ, $\tilde{\gamma}$) is sufficiently strong to ensure the simultaneous existence of stable healthy and diseased equilibria $\tilde{p}^h$ and $\tilde{p}^d$. We will find that the dynamical behaviour that emerges is significantly more complicated than that in the $R_0 > 1$ case covered by previous studies. In particular, many more stable states may exist, and propagation between ROIs may fail.

We will tackle the analysis of equation (4.1) in small steps. We start by analysing the simplest possible non-trivial network, namely the two-node network, in place of the 83-node connectome. We then study a second toy model, namely the 'star network' [87], which will shed some light on the influence of ROI-connectivity over the disease dynamics. Finally, we will study the critical seed size at different ROIs in the full connectome network. But first, we mention two useful properties of equation (4.1): its gradient structure and comparison property.

Gradient structure. Denoting $(\tilde{p}_1, \ldots, \tilde{p}_N)$ by $\tilde{\mathbf{p}}$, we can write equation (4.1) as a gradient system:

$$\frac{\mathrm{d}\tilde{\mathbf{p}}}{\mathrm{d}t} = -\nabla E(\tilde{\mathbf{p}}), \quad E(\tilde{\mathbf{p}}) := \frac{1}{2} D \sum_{i,j=1}^{N} w_{ij}(\tilde{p}_i - \tilde{p}_j)^2 - \sum_{i=1}^{N} \int_0^{\tilde{p}_i} f(\tilde{p}')\, \mathrm{d}\tilde{p}'. \tag{4.2}$$

It follows that all trajectories of equation (4.1) converge to an equilibrium of the system.[2]

Comparison principle. If a solution $\tilde{\mathbf{p}}^a \in \mathbb{R}^N$ of equation (4.1) is less than or equal to another solution $\tilde{\mathbf{p}}^b \in \mathbb{R}^N$ at every node, i.e. $\tilde{p}_i^a \leq \tilde{p}_i^b$ for all $i = 1, \ldots, N$, at $t = 0$, then it remains so for all $t > 0$. A proof is given in appendix C in the electronic supplementary material.

(a) The two-node network: the role of edge strength

The simplest non-trivial network has two nodes, in which case equation (4.1) takes the form

$$\frac{\mathrm{d}\tilde{p}_1}{\mathrm{d}t} = D(\tilde{p}_2 - \tilde{p}_1) + f(\tilde{p}_1) \tag{4.3a}$$

[2]This result follows from a theorem of Łojasiewicz [88] which guarantees convergence to equilibria in gradient systems whose potential/Lyapunov function is analytic and radially unbounded, the latter property guaranteeing the boundedness of forward orbits.

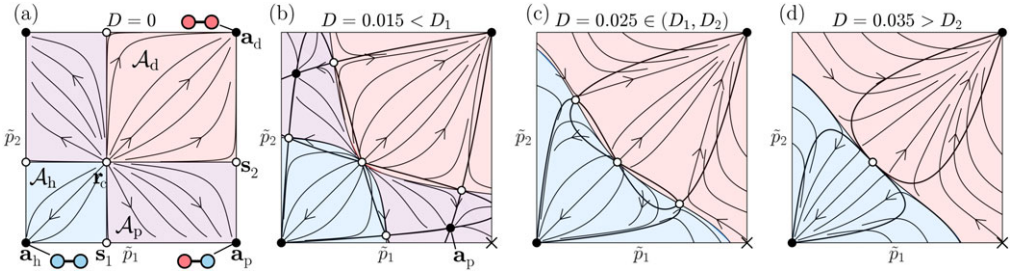

Figure 6. Phase plane of the two-node system (4.3) for four values of the diffusion coefficient D (given above each plot). Stable and unstable equilibria are indicated by black and white points, respectively, at the intersection of the two nullcline curves (for their labels, see the text). The domains of attraction $\mathcal{A}_h$, $\mathcal{A}_d$ and $\mathcal{A}_p$ are shaded blue, red and purple, respectively. Parameter values as in table 1.

and

$$\frac{\mathrm{d}\tilde{p}_2}{\mathrm{d}t} = D(\tilde{p}_1 - \tilde{p}_2) + f(\tilde{p}_2), \tag{4.3b}$$

where we have absorbed the edge weight w_{12} into D.

Phase plane. The phase plane of equation (4.3) is symmetric about the identity line $\tilde{p}_1 = \tilde{p}_2$ (unsurprisingly, given the symmetry of the network), and this line contains exactly three equilibria independent of $D \geq 0$, namely

$$\mathbf{a}_h = (\tilde{p}^h, \tilde{p}^h), \quad \mathbf{r}_c = (\tilde{p}^c, \tilde{p}^c) \quad \text{and} \quad \mathbf{a}_d = (\tilde{p}^d, \tilde{p}^d), \tag{4.4}$$

where $\tilde{p}^h < \tilde{p}^c < \tilde{p}^d$ are the three roots of the bistable reaction function $f(\tilde{p})$ (see figure 4d). The healthy and diseased equilibria, $\mathbf{a}_h$ and $\mathbf{a}_d$, are attractors, with domains of attraction denoted by $\mathcal{A}_h$ and $\mathcal{A}_d$ (blue and red regions in figure 6), while $\mathbf{r}_c$ is a repellor (either a saddle or an unstable node).

Inspection of equation (4.3) yields that all equilibria lie in $\mathcal{R} = [\tilde{p}^h, \tilde{p}^d] \times [\tilde{p}^h, \tilde{p}^d]$, and so by the system's gradient structure, every neighbourhood of $\mathcal{R}$ is an absorbing set. Thus, we restrict our attention to $\mathcal{R}$. It also follows from the comparison principle that the following square regions:

$$\mathcal{R}_h = (\tilde{p}^h, \tilde{p}^c) \times (\tilde{p}^h, \tilde{p}^c) \quad \text{and} \quad \mathcal{R}_d = (\tilde{p}^c, \tilde{p}^d) \times (\tilde{p}^c, \tilde{p}^d), \tag{4.5}$$

are positively invariant and that $\mathcal{R}_h \subseteq \mathcal{A}_h$ and $\mathcal{R}_d \subseteq \mathcal{A}_d$ for all $D \geq 0$. Therefore, no equilibria lie in the (open) squares $\mathcal{R}_h$ and $\mathcal{R}_d$.

Uncoupled case. When $D = 0$, the system has nine equilibria (figure 6a): the three given by equation (4.4), two *pinned* equilibria $\mathbf{a}_p$ and $R\mathbf{a}_p$ (attractors), and four saddles $\mathbf{s}_1$, $\mathbf{s}_2$, $R\mathbf{s}_1$, $R\mathbf{s}_2$, where

$$\mathbf{a}_p = (\tilde{p}^d, \tilde{p}^h), \quad \mathbf{s}_1 = (\tilde{p}^c, \tilde{p}^h) \quad \text{and} \quad \mathbf{s}_2 = (\tilde{p}^d, \tilde{p}^c), \tag{4.6}$$

and $R = \left(\begin{smallmatrix} 0 & 1 \\ 1 & 0 \end{smallmatrix}\right)$ reflects points through the identity line. We follow Kouvaris *et al.* [87] in calling $\mathbf{a}_p$ and $R\mathbf{a}_p$ pinned equilibria, since the disease is pinned at one node and unable to invade the other; we denote their domains of attraction by $\mathcal{A}_p$ and $R\mathcal{A}_p$ (purple regions in figure 6).

Bifurcations. Equilibria lie at intersections of the two nullclines, given by

$$D(\tilde{p}_1 - \tilde{p}_2) = f(\tilde{p}_1) \quad \text{and} \quad D(\tilde{p}_2 - \tilde{p}_1) = f(\tilde{p}_2). \tag{4.7}$$

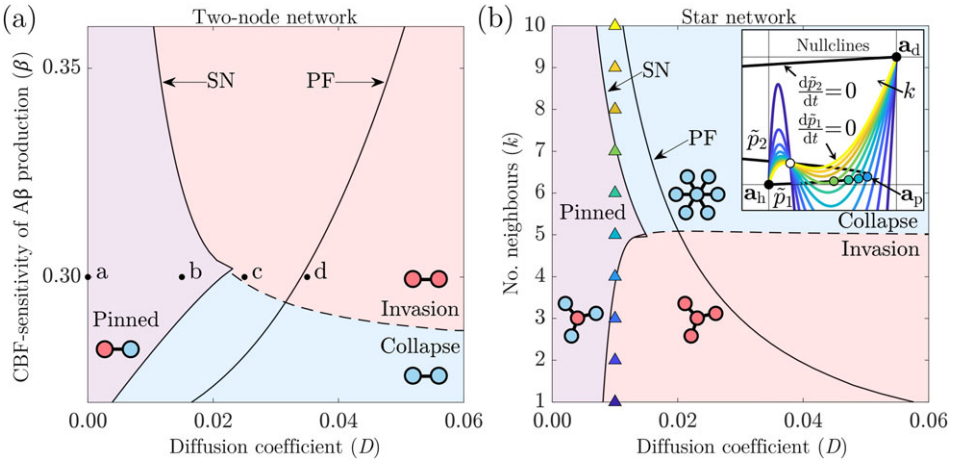

Figure 7. Phase diagrams for (a) the two-node network and (b) star network. Each parameter plane is divided into regions of disease invasion, collapse and pinning, according to whether $(\tilde{p}^d, \tilde{p}^h)$, marked by a cross in the phase planes of figure 6, is in $\mathcal{A}_d$, $\mathcal{A}_h$ or $\mathcal{A}_p$, respectively. Solid curves indicate branches of saddle-node and pitchfork (PF) bifurcations. Points a, b, c, d in (a) mark the parameter values used for the phase portraits in figure 6. Inset in (b) shows nullclines in the $(\tilde{p}_1, \tilde{p}_2)$ phase plane over a range of k values, each corresponding to a triangle on the $D = 0.01$ line in the phase diagram. The coloured circles in the inset of (b) indicate pinned equilibria, corresponding to triangles in the pinned region of the phase diagram (b). All parameters are as in table 1, except $\beta = 0.4$ in (b) (recall ϵ was eliminated by the QSSA).

For $D = 0$ (figure 6a), each nullcline consists of three parallel lines, and all intersections are transversal. Therefore, all nine equilibria persist (though perturbed) for sufficiently small $D > 0$ (figure 6b). In particular, disease pinning is possible when transport is weak.

At a threshold value $D = D_1$, $\mathbf{a}_p$ vanishes in a saddle-node bifurcation upon collision with one of the saddles $\mathbf{s}_i$. For $D > D_1$, only the healthy and diseased equilibria remain as attractors; compare figure 6b,c. A second bifurcation occurs at $D = D_2$, in which the remaining saddles $\mathbf{s}_j$ and $R\mathbf{s}_j$ collide with the repellor $\mathbf{r}_c$ in a supercritical pitchfork bifurcation, turning the unstable node $\mathbf{r}_c$ into a saddle; compare figure 6c,d. This second bifurcation, however, does not cause a sudden change in the domains of attraction of the healthy and diseased equilibria $\mathcal{A}_h$ and $\mathcal{A}_d$, and therefore does not affect the system's asymptotic behaviour.

The threshold values D_1 and D_2 depend on the system's other parameters, contained in the reaction function f. Their relationships with β (the sensitivity of the Aβ production rate to hypoperfusion) are indicated in figure 7a by the curves labelled 'SN' and 'PF', respectively.

Invasion. To investigate the dependence of disease invasion on D, we ask (similar to [87]) whether a pathogenic Aβ seed of size $\leq \tilde{p}^d$ placed at node 1 can spread to a healthy node 2. There are three possibilities:

— invasion: $(\tilde{p}^d, \tilde{p}^h) \in \mathcal{A}_d \implies$ invasion is possible for large enough seeds;
— pinning: $(\tilde{p}^d, \tilde{p}^h) \in \mathcal{A}_p \implies$ pinning, but not invasion, is possible for large enough seeds;
— collapse: $(\tilde{p}^d, \tilde{p}^h) \in \mathcal{A}_h \implies$ all seeds are extinguished; disease outbreak is not possible.

The point $(\tilde{p}^d, \tilde{p}^h)$ is marked by a cross in figure 6b–d, where it is in $\mathcal{A}_p$, $\mathcal{A}_d$, $\mathcal{A}_d$, respectively. Each of the phase planes (a, b, c, d) in figure 6 is also marked by a point in the phase diagram figure 7a.

Figure 7a shows how disease invasion in the two-node network is affected both by D and by the local protein kinetics $f(\tilde{p})$. In particular, when the sensitivity to hypoperfusion of the Aβ production rate, β, is large, invasion is possible for diffusivity stronger than D_1, whereas if β is small, $D > D_1$ leads to disease collapse.

A key insight of this section is that if the connection between two regions is sufficiently weak, then invasion from one to the other is not possible.

(b) The star network: the role of node degree

We now investigate the role of node degree (number of neighbours) in the dynamics of disease initiation and invasion. To this end, we perform an analysis of the so-called star network, comprising a central node ($i = 1$) connected by equally weighted edges to $k \geq 1$ neighbours [87].

We assume that all k peripheral nodes are initially healthy, and therefore have a common concentration $\tilde{p}_2$ for all $t \geq 0$; that is, the network's radial symmetry allows us to regard the peripheral nodes as identical. Therefore, we again have a planar system:

$$\frac{\mathrm{d}\tilde{p}_1}{\mathrm{d}t} = kD(\tilde{p}_2 - \tilde{p}_1) + f(\tilde{p}_1) \tag{4.8a}$$

and

$$\frac{\mathrm{d}\tilde{p}_2}{\mathrm{d}t} = D(\tilde{p}_1 - \tilde{p}_2) + f(\tilde{p}_2). \tag{4.8b}$$

The symmetry about the identity line $\tilde{p}_1 = \tilde{p}_2$ is lost when $k > 1$, but the dynamics of equation (4.8) is otherwise similar to that of the two-node network (4.3). For example, if the central node is seeded with pathogenic Aβ, then pinning occurs for sufficiently small D, therefore precluding invasion. Moreover, as D is increased, the same bifurcations (saddle-node and pitchfork) occur (figure 7b).

Increasing k hinders the ability of a seed placed at the central node to effect invasion of its neighbours. See figure 7b: for $D = 0.01$ (triangle markers), increasing k first precludes invasion in favour of pinning, and eventually leads to disease collapse. For large D, pinning cannot occur, and a critical value of k separates invasion from collapse ($k_{\mathrm{crit}} \approx (\tilde{p}^d - \tilde{p}^h)/\tilde{p}^c \approx 5$ in figure 7b).

Analysis of this toy network therefore suggests that highly connected brain regions are more resilient to seeds of pathogenic Aβ than poorly connected regions, and are less effective as bridgeheads for the invasion of neighbouring regions. We pursue this idea in more detail for the full connectome network below.

(c) The connectome network: critical seed size

Suppose all nodes in the N-node connectome network are in the healthy state $\tilde{p}^h$, and that node i is seeded with pathogenic Aβ. We ask: how large must the seed be to ensure escape from the healthy state $\mathbf{a}_h = (\tilde{p}^h, \ldots, \tilde{p}^h) \in \mathbb{R}^N$, thus triggering disease outbreak, and how is this threshold affected by Aβ transport? Precisely, we define the critical seed size associated with node i as

$$\tilde{p}_i^{\mathrm{crit}} = \min\{\tilde{p} > \tilde{p}^h : \mathbf{a}_h + (\tilde{p} - \tilde{p}^h)\mathbf{e}_i \notin \mathcal{A}_h\}. \tag{4.9}$$

First, we note that $\tilde{p}_i^{\mathrm{crit}} \geq \tilde{p}^c$ for all i and $D \geq 0$, with equality if and only if $D = 0$ (this follows from the comparison principle). Therefore, for small D, the critical seed size increases with respect to D.

If D is fixed, however, what is the effect of i's neighbours on $\tilde{p}_i^{\mathrm{crit}}$? A partial answer is obtained by comparing the critical seed size of each node to its weighted degree, $d_i := D\sum_{j=1}^N w_{ij}$. In figure 8b, we plot $\tilde{p}_i^{\mathrm{crit}}$, computed numerically given a small value of D, against d_i for all $N = 83$ nodes, and observe an increasing relationship. That is, highly connected nodes are more resilient to pathogenic seeding in the context of our model.

To gain further insight into this relationship, we can estimate $\tilde{p}_i^{\mathrm{crit}}$ via asymptotic expansion for small $D > 0$, the details of which are in appendix D in the electronic supplementary material. The resulting dependence is shown by the curve in figure 8b, and fits the numerically computed values well for small d_i.

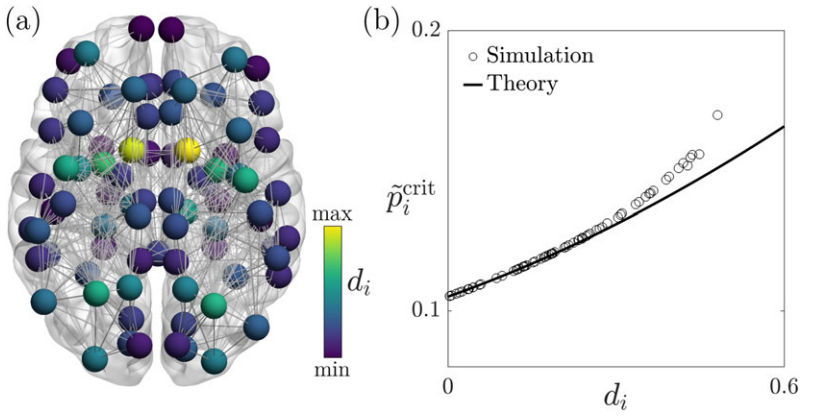

Figure 8. Critical seed size versus weighted degree. (a) The connectome network with nodes $i = 1, \ldots, 83$ coloured by weighted degree $d_i = D\sum_j w_{ij}$. (b) Critical seed size $\tilde{p}_i^{\text{crit}}$ versus weighted degree d_i; circular markers indicate values computed numerically for each node, and the curve indicates the asymptotic approximation derived in appendix D in the electronic supplementary material. Parameter values are as in table 1, and $D = 0.05$.

5. Disease initiation by vascular injury

So far, we have seen two theoretical mechanisms for disease initiation, namely an increase in R_0 above unity, and the introduction of a sufficiently large pathogenic seed.

In this section, we ask whether hypoperfusion of a localized brain region, due for example to embolic stroke or to atherosclerosis of the leptomeningeal vessels [15,39], may be sufficient to trigger Aβ pathology, without the need for a pathogenic seed. Specifically, we ask if a deficit in arterial blood supply is capable of destabilizing the healthy equilibrium $\mathbf{a}_h$.

We model this scenario as a proportional decrease $\Delta\Psi$ in perfusion pressure in a single node of the connectome network. For example, a value of $\Delta\Psi = 0.4$ represents a 40% decrease in perfusion pressure at the injured node. Because our simple model of blood flow in §2b(ii) is linear, the CBF rate in a brain region is proportional to the perfusion pressure in that region; therefore, $\Delta\Psi$ is also the proportional decrease in the normalized CBF rate q in the injured node. Recall from (2.14) the linear dependence of q on the open capillary fraction κ in a region with normal pressure ($\Delta\Psi = 0$), namely $q = \alpha(\kappa - 1) + 1$. Therefore, in the injured node, this relationship is scaled down to $q = (1 - \Delta\Psi)(\alpha(\kappa - 1) + 1)$, as shown in figure 9a.

Following the same model reduction and non-dimensionalization steps as in §2b(ii), we obtain new expressions for the Aβ production and clearance rates in the injured region, which now depend on $\Delta\Psi$:

$$\mu(\tilde{p}; \Delta\Psi) = (1 + \beta\Delta\Psi) + \beta(1 - \Delta\Psi)\frac{\tilde{p}}{c^{-1} + \tilde{p}},$$

$$\lambda(\tilde{p}; \Delta\Psi) = (1 - \gamma\Delta\Psi) - \gamma(1 - \Delta\Psi)\frac{\tilde{p}}{c^{-1} + \tilde{p}}$$

and

$$\tilde{\lambda}(\tilde{p}; \Delta\Psi) = (1 - \tilde{\gamma}\Delta\Psi) - \tilde{\gamma}(1 - \Delta\Psi)\frac{\tilde{p}}{c^{-1} + \tilde{p}}.$$

Substituting these expressions into formula (3.2) for the reaction function $f(\tilde{p})$, we obtain the *injured reaction function*, which we denote by $f_{\text{inj}}(\tilde{p}; \Delta\Psi)$; note $f_{\text{inj}}(\tilde{p}; 0) = f(\tilde{p})$. See figure 9b for $f_{\text{inj}}(\tilde{p}; \Delta\Psi)$ over a range of $\Delta\Psi$ values, and note $\partial_{\Delta\Psi} f_{\text{inj}} \geq 0$.

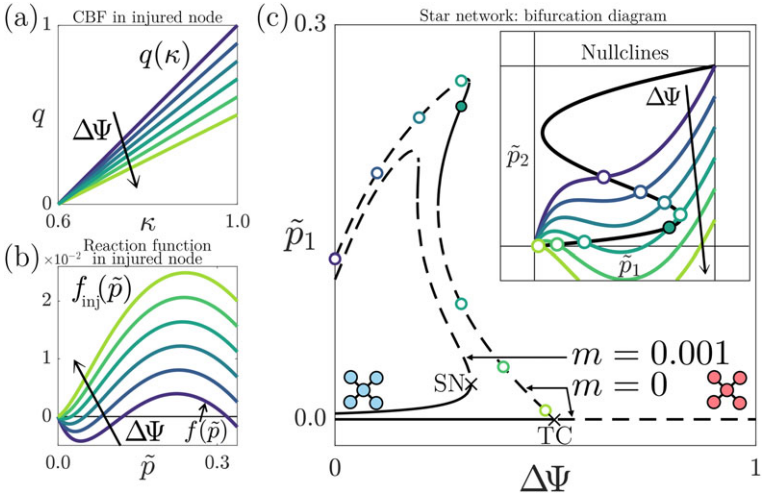

Figure 9. Effect of CBF supply deficit $\Delta\Psi$ on disease dynamics; the values of $\Delta\Psi$ in each panel are 0 (purple), 0.1, . . . , 0.5 (light green). (a) The normalized CBF rate q versus open capillary fraction κ (equation (2.14) with $\alpha = 2.5$). (b) The reaction function $f_{\text{inj}}(\tilde{p}; \Delta\Psi)$. (c) Bifurcation diagram for system (5.1) on the star network ($D = 0.02$), with respect to the bifurcation parameter $\Delta\Psi$; the transcritical and saddle-node bifurcations at the healthy equilibrium are marked by crosses. Inset: nullclines of the star network system. Parameter values as in table 1, except for $m = 0$.

Labelling the injured node as $i = 1$ without loss of generality, we obtain the following system:

$$\frac{\mathrm{d}\tilde{p}_1}{\mathrm{d}t} = f_{\text{inj}}(\tilde{p}_1; \Delta\Psi) + D\sum_{k=1}^{N} w_{1k}(\tilde{p}_k - \tilde{p}_1) \tag{5.1a}$$

and

$$\frac{\mathrm{d}\tilde{p}_j}{\mathrm{d}t} = f(\tilde{p}_j) + D\sum_{k=1}^{N} w_{jk}(\tilde{p}_k - \tilde{p}_j), \quad j \neq 1. \tag{5.1b}$$

If, by increasing $\Delta\Psi$, the healthy equilibrium $\mathbf{a}_h = (\tilde{p}^h, \ldots, \tilde{p}^h)$ becomes unstable, then disease outbreak ensues.

(a) An isolated injured node

If the injured node were isolated (no axonal connections), then equation (5.1) reduces to $\mathrm{d}\tilde{p}/\mathrm{d}t = f_{\text{inj}}(\tilde{p}; \Delta\Psi)$, so that stability of the healthy state $\tilde{p}^h$ is determined by the sign of the linear growth rate $r_{\text{inj}} := \partial_{\tilde{p}} f_{\text{inj}}(\tilde{p}^h; \Delta\Psi)$ alone. The linear growth rate is increasing with respect to $\Delta\Psi$, i.e. $\partial_{\Delta\Psi} r_{\text{inj}} > 0$; see figure 9b (in which $\tilde{p}^h = 0$). Therefore, the healthy state becomes less stable as the deficit in CBF supply becomes more severe. Stability is lost (and disease outbreak ensues) if the linear growth rate becomes positive at a critical $\Delta\Psi = \Delta\Psi^{\text{crit}}$.

Hard loss of stability. This threshold phenomenon is very similar to the increase of R_0 through unity in Prusiner's heterodimer model, as depicted in figure 2. Both are examples of transcritical bifurcation (with imperfection if $m > 0$). However, the loss of stability is *soft* in figure 2, whereas it is *hard* in the present case. That is, for $R_0 = 1 + \delta$ in Prusiner's heterodimer model, with $\delta \ll 1$, the diseased state $\tilde{p}^d$ is $O(\delta)$-close to the (now unstable) healthy state $\tilde{p}^h$—the transition to disease is smooth and gradual. However, for $\Delta\Psi$ just above $\Delta\Psi^{\text{crit}}$, the branch of diseased equilibria is far above $\tilde{p}^h$—the transition to disease is discontinuous and catastrophic.

To verify this fact, one shows in the latter case that the positive branch of equilibria near the transcritical bifurcation is *subcritical* (below $\Delta\Psi^{\text{crit}}$); see figure 9b, where the middle root

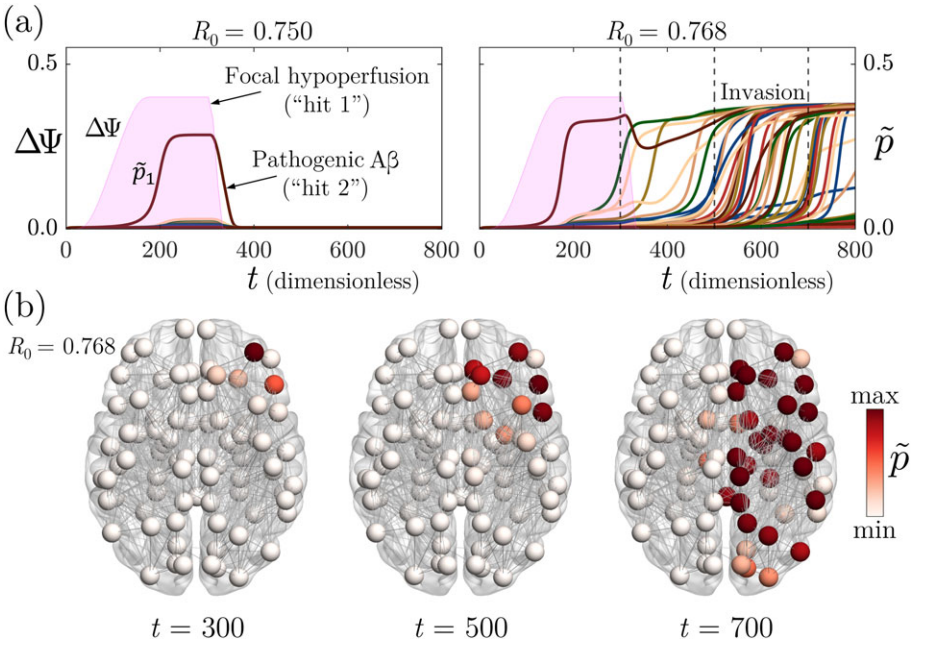

Figure 10. Two-hit mechanism for disease initiation. (a) Focal hypoperfusion following vascular injury ('hit 1', left axis) destabilizes the disease-free state $\mathbf{a}_h$, causing localized outbreak of pathogenic Aβ ('hit 2', right axis), which may or may not spread (right and left panels of (a), respectively). The shaded area indicates the prescribed time course of the arterial supply deficit $\Delta\Psi$ at the injured brain region, and the curves indicate the evolution of pathogenic Aβ concentration $\tilde{p}_i$ at each node $i = 1, \ldots, 83$. Owing to the system's hysteresis, full restoration of the arterial blood supply (i.e. $\Delta\Psi \searrow 0$) may not be sufficient to stop the spread. (b) Disease spread from the injury site: disease distribution at $t = 300, 500, 700$ in right-hand panel of (a), marked there by dashed lines. Parameters as in table 1 except $R_0 = 0.768$, not 0.75, in right-hand panel of (a) and in (b), and $D = 0.2$.

of f_{inj} *decreases* through $\tilde{p}^h = 0$ as $\Delta\Psi$ *increases* through $\Delta\Psi^{\text{crit}} \approx 0.35$. Analytically, one can establish subcriticality of the positive branch by verifying (see Glendinning [89, §8.4]) that $\partial^2_{\tilde{p}} f_{\text{inj}}(\tilde{p}^h; \Delta\Psi^{\text{crit}}) > 0$ and $\partial_{\Delta\Psi}\partial_{\tilde{p}} f_{\text{inj}}(\tilde{p}^h; \Delta\Psi^{\text{crit}}) > 0$.

(b) Star network with injured central node

Suppose next that the injured node is the central node of a star network with k neighbours, so that the reaction function of the central node is $f_{\text{inj}}(\tilde{p}; \Delta\Psi)$, and that of the k peripheral nodes is $f(\tilde{p}) = f_{\text{inj}}(\tilde{p}; 0)$. Denote the linear growth rates at the injured and un-injured nodes by $r_{\text{inj}} := \partial_{\tilde{p}} f_{\text{inj}}(\tilde{p}^h; \Delta\Psi)$ and $r_0 := \partial_{\tilde{p}} f(\tilde{p}^h)$, respectively (recall $r_0 < 0$).

Connectivity imparts resilience. Stability of the healthy state $\mathbf{a}_h \in \mathbb{R}^2$ is now determined by r_{inj} and r_0. By analysing the star network system (4.8*a*) with $f(\tilde{p}_1)$ replaced with $f_{\text{inj}}(\tilde{p}_1; \Delta\Psi)$, one can verify here that r_{inj} must now exceed $r^{\text{crit}}_{\text{inj}} := Dkr_0/(r_0 - D)$ in order to destabilize $\mathbf{a}_h$. This threshold is increasing with respect to both D and k. If either is zero, then $r^{\text{crit}}_{\text{inj}} = 0$ and we are back to the isolated node case of §5a. At the other extreme, if $D \to \infty$, then $r^{\text{crit}}_{\text{inj}} = -kr_0 > 0$. In short, highly connected nodes are more resilient than poorly connected nodes.

If $\Delta\Psi$ increases to such an extent that r_{inj} exceeds the above threshold (recall from §5a that $\partial_{\Delta\Psi} r_{\text{inj}} > 0$), then disease outbreak ensues. It is straightforward to show that, as in the isolated node case, the loss of stability is hard; see figure 9c and note that the positive branch near 'TC' is subcritical.

(c) Connectome network with an injured node

The linearization of system (5.1) (in its full generality) about $\mathbf{a}_h \in \mathbb{R}^N$ is $\mathrm{d}\tilde{\mathbf{p}}/\mathrm{d}t = J\tilde{\mathbf{p}}$, where J is the Jacobian matrix

$$J = M - DL, \tag{5.2}$$

with $M = \mathrm{diag}(r_{\mathrm{inj}}, r_0, \ldots, r_0)$ and L is the graph Laplacian of the connectome network (see electronic supplementary material for information on the graph Laplacian). We denote the largest of J's eigenvalues, all of which are real, by σ_J. The healthy equilibrium is stable if $\sigma_J < 0$, and unstable if $\sigma_J > 0$.

We obtain the following bounds on σ_J:

$$\sigma_J \in (r_{\mathrm{inj}} - d_1, r_{\mathrm{inj}}), \tag{5.3}$$

where $d_1 = D\sum_{k=1}^{N} w_{1k}$ (weighted degree of the injured node). Indeed, $\sigma_J = \max_{||\mathbf{u}||=1} \mathbf{u}^{\mathsf{T}} J\mathbf{u}$, whence $\sigma_J > \mathbf{e}_1^{\mathsf{T}} J\mathbf{e}_1 = r_{\mathrm{inj}} - d_1$, and from equation (5.2) we have $\sigma_J < \sigma_M + \sigma_{-DL} = r_{\mathrm{inj}}$, where we have used the fact that the largest eigenvalue of $-L$ is 0, as is true for any graph Laplacian. From equation (5.3), we obtain bounds on the critical value of $r_{\mathrm{inj}} = r_{\mathrm{inj}}^{\mathrm{crit}}$ (for which $\sigma_J = 0$) above which $\mathbf{a}_h$ is unstable:

$$r_{\mathrm{inj}}^{\mathrm{crit}} \in (0, d_1). \tag{5.4}$$

This upper bound indicates the positive effect of connectivity on resilience, as in the star network case. If $\Delta\Psi$ increases to such an extent that r_{inj} rises above $r_{\mathrm{inj}}^{\mathrm{crit}}$, then $\mathbf{a}_h$ is destabilized in a transcritical bifurcation (with imperfection if $m > 0$), and we expect the loss of stability to be hard as in §5a and b.

Simulation: injury-induced disease outbreak. To complement the analysis above, we ran a numerical simulation in which we increased $\Delta\Psi$ slowly from 0 to 0.4 in a single node of the connectome network, namely the rostral middle frontal gyrus, near the top of the right hemisphere in figure 10b.

Whereas initial disease outbreak is decided by the (linear) stability of the healthy equilibrium alone, progression of the disease (e.g. whether or not spatial propagation ensues) is determined by the complex dynamics of system (5.1) in all its nonlinearity. In the left-hand panel of figure 10a, $\mathbf{a}_h$ indeed undergoes a hard loss of stability, but invasion of neighbouring regions does not follow—disease outbreak occurs locally, but is pinned at the injured node. In the right-hand panel of figure 10a, R_0 has a slightly higher value, and this time invasion is successful. Moreover, returning $\Delta\Psi$ to zero following outbreak need not be sufficient to quell disease progression, as seen in the right-hand panel of figure 10a. This irreversibility is due to the system's hysteretic property, already observed in §3.

To summarize, this section has demonstrated, in the context of our model, how a focal deficit in arterial blood supply, if sufficiently severe, can trigger prion-like accumulation and spatial propagation of pathogenic Aβ without the need for an initial seed.

6. Discussion

The role of cerebrovascular disease in neurodegeneration has been debated for over a century [17,90]. In the last 30 years, several mechanisms have emerged through which Aβ and the brain's vessels may influence each other: hypoperfusion and BBB breakdown exacerbate Aβ accumulation [33–36], whereas Aβ is vasoconstrictive [28,29], pro-atherogenic [17,91], and therefore inhibits CBF. In particular, recent experiments have established that pathogenic forms of Aβ constrict capillaries in AD by causing pericytes to contract [14]. Here, we have constructed a mathematical model that integrates Aβ-induced capillary constriction (and its effect on CBF) with the prion-like property of Aβ, with the goal of gaining mechanistic insight into their combined effect on disease initiation and spreading. We summarize the model assumptions in table 2. Below, we discuss the key insights that have emerged from the model's analysis, and several limitations.

Table 2. Summary of model assumptions, which fall into two categories, namely biological premises (Bio.) and modelling simplifications (Mod.), along with the section of the present paper in which the assumption is invoked (§), and sources.

assumption	type	§	source
Aβ is prion-like.	Bio.	2a	[4–6,8,9]
Aβ production rate increases when CBF decreases.	Bio.	2a	[33–35]
Aβ clearance rate decreases when CBF decreases.	Bio.	2a	[30,36]
clearance rate of pathogenic Aβ $<$ clearance rate of normal Aβ.	Bio.	3b	[99]
pericytes contract & constrict capillaries when exposed to Aβ.	Bio.	2b(i)	[14]
brain capillary networks are degree-three & without community structure.	Bio.	2b(ii)	[67]
brain microvasculature behaves as a disjoint union of degree-three RRGs with uniform edge conductances, fed by a single arteriole and drained by a single venule.	Mod.	2b(ii)	[54]
flow through capillary network obeys Kirchhoff's and Ohm's Laws.	Mod.	2b(ii)	[70]
axonal transport of Aβ is bi-directional.	Bio.	4	[78]

(a) Key insights

Bistability, critical seed size, hysteresis. Eigen [60], in one of the earliest modelling studies on 'prionics', dismissed Prusiner's classic heterodimer model as implausible, as 'either there is no infection at all … or a spontaneous outbreak of the disease occurs… in every case'. This criticism, shared by others [57,61], pertains to the absence of a threshold phenomenon, a 'knife-edge' [61], separating disease outbreak from the disease-free state that most people, thankfully, never leave.

By incorporating putative interaction mechanisms between Aβ and microvascular damage into the heterodimer model, we have shown that metastability of the healthy state is possible. Specifically, should the prion mechanism alone be incapable of generating disease outbreak ($R_0 < 1$), but the Aβ-microvascular coupling is sufficiently strong (β, γ, $\tilde{\gamma}$, c sufficiently large), then bistable dynamics can emerge, in which case seeds of pathogenic protein must exceed a minimal threshold to trigger disease outbreak.

Another consequence of the Aβ-vascular feedback is that an increase of R_0 through unity, for example due to age-related decline in the Aβ degradation rate [64], now precipitates a *hard* loss of stability by the healthy state. The biological relevance of this change from soft to hard is at least twofold. First, the prion-like disease outbreak is sudden and catastophic in the hard case (figures 4b and 9), unlike the soft transition in Prusiner's heterodimer model (figure 2). Second, the hard loss in stability results in hysteresis, implying that the pathology, once triggered, is likely very difficult to eliminate, thus making preventative therapies (aimed at keeping patients in the subcritical parameter regime) preferable to post-onset therapy. Examples could include the lowering of R_0, e.g. by increasing Aβ clearance, or of the contraction ratio c (table 1), e.g. by blocking Aβ-induced generation of ROS (modelled here in §2b(i)), as already proposed by Nortley *et al.* [14]. Another preventative strategy would be to monitor and treat cerebral hypoperfusion prophylactically before other AD pathology is present (in order to keep $\Delta\Psi$ below $\Delta\Psi^{\mathrm{crit}}$; see figures 9 and 10).

Prion models exhibiting bistable dynamics have been proposed on phenomenological grounds [92,93], and based on an assumption of nucleation-dependent aggregation [61]. Our results indicate that Aβ-induced vascular damage and its feedback onto the kinetics of Aβ comprise another route to bistability.

Two-hit vascular hypothesis. A vascular two-hit hypothesis for AD has existed for at least twenty years, which proposes that cerebrovascular damage is the initial trigger of AD pathology, antecedent to Aβ accumulation [15,20,36,40]. In §5, we presented a theoretical manifestation of this

hypothesis, demonstrating how a focal decline in arterial blood supply, if it surpasses a threshold, can induce a hard loss of stability by the disease-free state, leading to an outbreak of pathology even in the absence of an initial pathogenic seed (figure 9). To our knowledge, this is the first attempt to formalize and analyse the two-hit hypothesis mathematically.

This theoretical mechanism of vascular-injury-induced disease initiation is consistent with experimental studies in mouse models of AD. For example, focal cerebral hypoperfusion, induced by the targeted occlusion of penetrating cortical arterioles, has been shown to increase the number of Aβ plaques in the infarcted region [94]. Similarly, global chronic cerebral hypoperfusion, induced by bilateral common carotid artery stenosis, has been found to shift the equilibrium of Aβ toward its pathogenic form [95]. It is our hope that the results of §5 (particularly the presence of a threshold effect and a hard loss of stability) will help to supply mechanistic insight to these experimental findings and contribute to the refinement of the two-hit vascular hypothesis.

Complex spatial dynamics. In monostable spatially extended models of prion-like behaviour (such as Fisher's equation and the diffusive heterodimer model), every pathogenic seed, independent of size and location, leads to the eventual invasion of the entire domain [46,47,53,55,56,86]. That is, these models imply that the uniformly diseased brain is a global attractor.

In a bistable regime, however, spatial invasion is not straightforward, as has been shown for bistable dynamics on generic networks [87,96–98]. By analysing simple model networks in §4a and b, we found that propagation fails if edges are too weak (figures 6 and 7), representing weak axonal connectivity, which enables stable, spatially heterogeneous steady states to emerge, i.e. pinned states (figure 6).

The size of a pathogenic seed required to trigger local outbreak in a well-connected region is higher than that in a poorly connected region. The stronger effect of diffusion at the well-connected region is stabilizing, as it is capable of evacuating more pathogenic proteins to neighbouring regions, whose clearance capacity can then be exploited to suppress disease outbreak (figure 8; see also [51]). Together, these observations indicate that spatial propagation (whether it occurs, along what paths, towards what asymptotic state) is complex when the disease-free state is metastable, in contrast to the case where it is unstable [47,49,55,59].

(b) Limitations

In considering the results, certain limitations should be borne in mind, including the following.

(1) Our model neglects countless important features of AD pathogenesis, e.g. τP accumulation, neuroinflammation, neuron death, and the myriad interdependences between these and other pathways. In focusing on the combined effect of two specific aspects of AD, namely the prion-like kinetics of Aβ and microvascular damage, we make no claim regarding their relative importance in comparison to the pathways left unaddressed. The goal of the model has been to investigate the theoretical implications of the two-way coupling between these two pathways, but it could be extended to incorporate others. A natural pathway to include would be that of τP. Hyperphosphorylation of τP is downstream of Aβ accumulation in AD [30], the implications of which have been explored with mathematical modelling [49]. Also, ischaemia triggers τP hyperphosphorylation independent of Aβ [30]. These interactions could be incorporated in a straightforward manner into our model. Nonetheless, to quote Fisher, 'the effects of all such complications can only be discussed by reference to the course of events when they are absent' [100].

(2) We have modelled the transport of proteins along axons as a simple diffusion process in the connectome network, following Raj *et al.* [79] and others [47,101]. This approach captures the topology of the connectome, which is important for protein spreading

patterns [47,55,86], but is not derived from a mechanistic description of Aβ molecular movement, as a continuum diffusion model may be interpreted [46].

(3) We have modelled the brain's microvasculature as a collection of small independent capillary networks, so that capillary damage in one brain region does not affect the CBF rate in other regions. Though we believe this minimal model to be reasonable for our purposes, the notion that the brain's capillary bed is organized as a collection of 'largely autonomous modules, each sourced by one or more penetrating arterioles and drained by one or more penetrating venules' has been challenged [102]. A more sophisticated approach would treat the capillary bed as a brain-wide network, fed and drained by many penetrating vessels from the pial surface.

One approach that would address limitations (2) and (3) would be to model the brain as a continuum in which Aβ can diffuse, as in [46,53], and the brain's microvasculature as a continuous porous medium whose spatially varying permeability field depends on the local concentration of pathogenic Aβ, consistent with Aβ-induced capillary constriction. The result would be a coupled system of partial differential equations, probably of parabolic-elliptic type, on a complex geometry. This approach would have the benefit of being derivable from mechanistic physical principles (by coarse-graining the underlying capillary bed), though at the price of greater computational expense and lesser analytic tractability compared with the network model presented here.

Data accessibility. The data are provided in the electronic supplementary material [103].

Declaration of AI use. We have not used AI-assisted technologies in creating this article.

Conflict of interest declaration. We declare we have no competing interests.

Authors' contributions. A.A.: conceptualization, data curation, formal analysis, funding acquisition, investigation, methodology, project administration, resources, software, supervision, validation, visualization, writing—original draft, writing—review and editing; T.B.T.: conceptualization, formal analysis, methodology, visualization, writing—original draft, writing—review and editing; H.O.: conceptualization, formal analysis, investigation, methodology, visualization, writing—original draft, writing—review and editing; S.L.: conceptualization, formal analysis, supervision, writing—original draft, writing—review and editing; A.G.: conceptualization, formal analysis, funding acquisition, investigation, methodology, project administration, resources, supervision, writing—original draft, writing—review and editing.

All authors gave final approval for publication and agreed to be held accountable for the work performed therein.

Funding. The work of A.A. was supported by the Clarendon Fund, the benefactors of the Foley-Béjar Scholarship, the Irish Fulbright Commission, Roche, and the Engineering and Physical Sciences Research Council (grant no. EP/S024093/1). The work of A.G. was supported by the Engineering and Physical Sciences Research Council (grant no. EP/R020205/1). The work of T.B.T. was partially supported by EP/R020205/1 to A.G. and partially supported by the National Science Foundation under grant no. NSF 2325276 to T.B.T. The work of S.L. was partially supported by the NIH-NINDS (RF1NS110054), the Leducq Foundation (23CVD03) and Agence Nationale de la Recherche (J452IMF23174).

Acknowledgements. We thank Dr Anusha Mishra for helpful discussions on the interplay between stroke and AD pathology.

References

1. Jack CR *et al.* 2018 NIA-AA Research Framework: toward a biological definition of Alzheimer's disease. *Alzheimer's Dement.* **14**, 535–562. (doi:10.1016/j.jalz.2018.02.018)
2. Knowles TP, Vendruscolo M, Dobson CM. 2014 The amyloid state and its association with protein misfolding diseases. *Nat. Rev. Mol. Cell Biol.* **15**, 384–396. (doi:10.1038/nrm3810)
3. Chen GF, Xu TH, Yan Y, Zhou YR, Jiang Y, Melcher K, Xu E. 2017 Amyloid beta: structure, biology and structure-based therapeutic development. *Acta Pharmacol. Sin.* **38**, 1205–1235. (doi:10.1038/aps.2017.28)
4. Jucker M, Walker LC. 2011 Pathogenic protein seeding in Alzheimer disease and other neurodegenerative disorders. *Ann. Neurol.* **70**, 532–540. (doi:10.1002/ana.22615)

5. Jucker M, Walker LC. 2013 Self-propagation of pathogenic protein aggregates in neurodegenerative diseases. *Nature* **501**, 45–51. (doi:10.1038/nature12481)
6. Prusiner SB. 2013 Biology and genetics of prions causing neurodegeneration. *Annu. Rev. Genet.* **47**, 601–623. (doi:10.1146/annurev-genet-110711-155524)
7. Walker LC, Jucker M. 2015 Neurodegenerative diseases: expanding the Prion Concept. *Annu. Rev. Neurosci.* **38**, 87–103. (doi:10.1146/annurev-neuro-071714-033828)
8. Goedert M. 2015 Alzheimer's and Parkinson's diseases: the prion concept in relation to assembled Aβ, tau, and α-synuclein. *Science* **349**, 61–69. (doi:10.1126/science.1255555)
9. Jucker M, Walker LC. 2018 Propagation and spread of pathogenic protein assemblies in neurodegenerative diseases. *Nat. Neurosci.* **21**, 1341–1349. (doi:10.1038/s41593-018-0238-6)
10. Cortes-Canteli M, Iadecola C. 2020 Alzheimer's disease and vascular aging: JACC focus seminar. *J. Am. Coll. Cardiol.* **75**, 942–951. (doi:10.1016/j.jacc.2019.10.062)
11. Editorial. 2012 A united approach to vascular disease and neurodegeneration. *Lancet Neurol.* **11**, 293. (doi:10.1016/S1474-4422(12)70050-9)
12. Iadecola C. 2013 The pathobiology of vascular dementia. *Neuron* **80**, 844–866. (doi:10.1016/j.neuron.2013.10.008)
13. Iturria-Medina Y, Sotero RC, Toussaint PJ, Mateos-Pérez JM, Evans AC, Disease Neuroimaging Initiative The Alzheimer's. 2016 Early role of vascular dysregulation on late-onset Alzheimer's disease based on multifactorial data-driven analysis. *Nat. Commun.* **7**, 11934. (doi:10.1038/ncomms11934)
14. Nortley R *et al.* 2019 Amyloid β oligomers constrict human capillaries in Alzheimer's disease via signaling to pericytes. *Science* **365**, eaav9518. (doi:10.1126/science.aav9518)
15. Roher AE, Esh C, Rahman A, Kokjohn TA, Beach TG. 2004 Atherosclerosis of cerebral arteries in Alzheimer disease. *Stroke* **35**, 2623–2627. (doi:10.1161/01.STR.0000143317.70478.b3)
16. Faraco G, Iadecola C. 2013 Hypertension: a harbinger of stroke and dementia. *Hypertension* **62**, 810–817. (doi:10.1161/HYPERTENSIONAHA.113.01063)
17. Iadecola C. 2004 Neurovascular regulation in the normal brain and in Alzheimer's disease. *Nat. Rev. Neurosci.* **5**, 347–360. (doi:10.1038/nrn1387)
18. Deschaintre Y, Richard F, Leys D, Pasquier F. 2009 Treatment of vascular risk factors is associated with slower decline in Alzheimer disease. *Neurology* **73**, 674–680. (doi:10.1212/WNL.0b013e3181b59bf3)
19. Sörös P, Whitehead S, Spence JD, Hachinski V. 2013 Opinion: antihypertensive treatment can prevent stroke and cognitive decline. *Nat. Rev. Neurol.* **9**, 174–178. (doi:10.1038/nrneurol.2012.255)
20. Sweeney MD, Sagare AP, Zlokovic BV. 2018 Blood-brain barrier breakdown in Alzheimer disease and other neurodegenerative disorders. *Nat. Rev. Neurol.* **14**, 133–150. (doi:10.1038/nrneurol.2017.188)
21. de Jong DL, De Heus RA, Rijpma A, Donders R, Olde Rikkert MG, Günther M, Lawlor BA, Van Osch MJ, Claassen JA. 2019 Effects of nilvadipine on cerebral blood flow in patients with Alzheimer disease: a randomized trial. *Hypertension* **74**, 413–420. (doi:10.1161/HYPERTENSIONAHA.119.12892)
22. McKhann G, Drachman D, Folstein M, Katzman R. 1984 Clinical diagnosis of Alzheimer's disease. *Neurology* **34**, 939. (doi:10.1212/WNL.34.7.939)
23. Khachaturian ZS. 1985 Diagnosis of Alzheimer's disease: neuropsychological testing. *Arch. Neurol.* **4**, 1097–1105. (doi:10.1001/archneur.1985.04060100083029)
24. Hachinski VC, Lassen NA, Marshall J. 1974 Multi-infarct dementia: a cause of mental deterioration in the elderly. *Lancet* **304**, 207–210. (doi:10.1016/s0140-6736(74)91496-2)
25. Román GC *et al.* 1993 Vascular dementia: diagnostic criteria for research studies—report of the NINDS-AIREN international workshop. *Neurology* **43**, 250–260. (doi:10.1212/wnl.43.2.250)
26. Gorelick PB *et al.* 2011 Vascular contributions to cognitive impairment and dementia: a statement for healthcare professionals from the American Heart Association/American Stroke Association. *Stroke* **42**, 2672–2713. (doi:10.1161/STR.0b013e3182299496)
27. Corriveau RA, Bosetti F, Emr M, Gladman JT, Koenig JI, Moy CS, Pahigiannis K, Waddy SP, Koroshetz W. 2016 The science of vascular contributions to cognitive impairment and dementia (VCID): a framework for advancing research priorities in the cerebrovascular biology of cognitive decline. *Cell. Mol. Neurobiol.* **36**, 281–288. (doi:10.1007/s10571-016-0334-7)

28. Thomas T, Thomas G, McLendon C, Sutton T, Mullan M. 1996 β-Amyloid-mediated vasoactivity and vascular endothelial damage. *Nature* **380**, 168–171. (doi:10.1038/380168a0)
29. Niwa K, Porter VA, Kazama KE, Cornfield D, Carlson GA, Iadecola C. 2001 Aβ-peptides enhance vasoconstriction in cerebral circulation. *Am. J. Physiol. Heart Circ. Physiol.* **281**, 2417–2424. (doi:10.1152/ajpheart.2001.281.6.h2417)
30. Korte N, Nortley R, Attwell D. 2020 Cerebral blood flow decrease as an early pathological mechanism in Alzheimer's disease. *Acta Neuropathol.* **140**, 793–810. (doi:10.1007/s00401-020-02215-w)
31. Hartmann DA, Coelho-Santos V, Shih AY. 2022 Pericyte control of blood flow across microvascular zones in the central nervous system. *Annu. Rev. Physiol.* **84**, 331–354. (doi:10.1146/annurev-physiol-061121-040127)
32. Cruz Hernández JC *et al.* 2019 Neutrophil adhesion in brain capillaries reduces cortical blood flow and impairs memory function in Alzheimer's disease mouse models. *Nat. Neurosci.* **22**, 413–420. (doi:10.1038/s41593-018-0329-4)
33. Sun X, He G, Qing H, Zhou W, Dobie F, Cai F, Staufenbiel M, Huang LE, Song W. 2006 Hypoxia facilitates Alzheimer's disease pathogenesis by up-regulating BACE1 gene expession. *Proc. Natl Acad. Sci. USA* **103**, 18 727–18 732. (doi:10.1073/pnas.0606298103)
34. Shi J, Yang SH, Stubley L, Day AL, Simpkins JW. 2000 Hypoperfusion induces overexpression of β-amyloid precursor protein mRNA in a focal ischemic rodent model. *Brain Res.* **853**, 1–4. (doi:10.1016/S0006-8993(99)02113-7)
35. Kalaria RN, Bhatti SU, Palatinsky EA, Pennington DH, Shelton ER, Chan HW, Perry G, Lust WD. 1993 Accumulation of the β amyloid precursor protein at sites of ischemic injury in rat brain. *NeuroReport* **4**, 211–214. (doi:10.1097/00001756-199302000-00025)
36. Sagare AP, Bell RD, Zlokovic BV. 2012 Neurovascular dysfunction and faulty amyloid β-peptide clearance in Alzheimer disease. *Cold Spring Harbor Perspect. Med.* **2**, 1–18. (doi:10.1101/cshperspect.a011452)
37. Shibata M *et al.* 2000 Clearance of Alzheimer's amyloid-β_{1-40} peptide from brain by LDL receptor-related protein-1 at the blood-brain barrier. *J. Clin. Invest.* **106**, 1489–1499. (doi:10.1172/JCI10498)
38. Tarasoff-Conway JM *et al.* 2015 Clearance systems in the brain—implications for Alzheimer disease. *Nat. Rev. Neurol.* **11**, 457–470. (doi:10.1038/nrneurol.2015.119)
39. Dong S, Maniar S, Manole MD, Sun D. 2018 Cerebral hypoperfusion and other shared brain pathologies in ischemic stroke and Alzheimer's disease. *Transl. Stroke Res.* **9**, 238–250. (doi:10.1007/s12975-017-0570-2)
40. Kisler K, Nelson AR, Montagne A, Zlokovic BV. 2017 Cerebral blood flow regulation and neurovascular dysfunction in Alzheimer disease. *Nat. Rev. Neurosci.* **18**, 419–434. (doi:10.1038/nrn.2017.48)
41. Tomski SJ, Murphy RM. 1992 Kinetics of aggregation of synthetic β-amyloid peptide. *Arch. Biochem. Biophys.* **294**, 630–638. (doi:10.1016/0003-9861(92)90735-F)
42. Pallitto MM, Murphy RM. 2001 A mathematical model of the kinetics of β-amyloid fibril growth from the denatured state. *Biophys. J.* **81**, 1805–1822. (doi:10.1016/S0006-3495(01)75831-6)
43. Craft DL, Wein LM, Selkoe DJ. 2002 A mathematical model of the impact of novel treatments on the *Aβ* burden in the Alzheimer's brain, CSF and plasma. *Bull. Math. Biol.* **64**, 1011–1031. (doi:10.1006/bulm.2002.0304)
44. Hall D, Edskes H. 2004 Silent prions lying in wait: a two-hit model of prion/amyloid formation and infection. *J. Mol. Biol.* **336**, 775–786. (doi:10.1016/j.jmb.2003.12.004)
45. Bertsch M, Franchi B, Marcello N, Tesi MC, Tosin A. 2017 Alzheimer's disease: a mathematical model for onset and progression. *Math. Med. Biol.* **34**, 193–214. (doi:10.1093/imammb/dqw003)
46. Weickenmeier J, Kuhl E, Goriely A. 2018 Multiphysics of prionlike diseases: progression and atrophy. *Phys. Rev. Lett.* **121**, 158101. (doi:10.1103/PhysRevLett.121.158101)
47. Fornari S, Schäfer A, Jucker M, Goriely A, Kuhl E. 2019 Prion-like spreading of Alzheimer's disease within the brain's connectome. *J. R. Soc. Interface* **16**, 20190356. (doi:10.1098/RSIF.2019.0356)
48. Fornari S, Schäfer A, Kuhl E, Goriely A. 2020 Spatially-extended nucleation-aggregation-fragmentation models for the dynamics of prion-like neurodegenerative protein-spreading in the brain and its connectome. *J. Theor. Biol.* **486**, 110102. (doi:10.1016/j.jtbi.2019.110102)

49. Thompson TB, Chaggar P, Kuhl E, Goriely A. 2020 Protein-protein interactions in neurodegenerative diseases: a conspiracy theory. *PLoS Comput. Biol.* **16**, e1008267. (doi:10.1371/journal.pcbi.1008267)
50. Bertsch M, Franchi B, Meacci L, Primicerio M, Tesi MC. 2021 The amyloid cascade hypothesis and Alzheimer's disease: a mathematical model. *Eur. J. Appl. Math.* **32**, 749–768. (doi:10.1017/S0956792520000339)
51. Brennan G, Thompson T, Oliveri H, Rognes M, Goriely A. 2023 The role of clearance in neurodegenerative diseases. *SIAM J. Appl. Math.* **84**, S172–S198. (doi:10.1137/22M1487801)
52. Prusiner SB. 1991 Molecular biology of prion diseases. *Science* **252**, 1515–1522. (doi:10.1126/science.1675487)
53. Weickenmeier J, Jucker M, Goriely A, Kuhl E. 2019 A physics-based model explains the prion-like features of neurodegeneration in Alzheimer's disease, Parkinson's disease, and amyotrophic lateral sclerosis. *J. Mech. Phys. Solids* **124**, 264–281. (doi:10.1016/j.jmps.2018.10.013)
54. Goirand F, Le Borgne T, Lorthois S. 2021 Network-driven anomalous transport is a fundamental component of brain microvascular dysfunction. *Nat. Commun.* **12**, 7295. (doi:10.1038/s41467-021-27534-8)
55. Matthäus F. 2006 Diffusion versus network models as descriptions for the spread of prion diseases in the brain. *J. Theor. Biol.* **240**, 104–113. (doi:10.1016/j.jtbi.2005.08.030)
56. Payne RJ, Krakauer DC. 1998 The spatial dynamics of prion disease. *Proc. R. Soc. Lond. B* **265**, 2341–2346. (doi:10.1006/jtbi.1997.0627)
57. Masel J, Jansen VA, Nowak MA. 1999 Quantifying the kinetic parameters of prion replication. *Biophys. Chem.* **77**, 139–152. (doi:10.1016/S0301-4622(99)00016-2)
58. Drazin PG. 1992 *Nonlinear systems*. Cambridge Texts in Applied Mathematics. Cambridge, UK: Cambridge University Press.
59. Alexandersen CG, de Haan W, Bick C, Goriely A. 2023 A multi-scale model explains oscillatory slowing and neuronal hyperactivity in Alzheimer's disease. *J. R. Soc. Interface* **20**, 20220607. (doi:10.1098/rsif.2022.0607)
60. Eigen M. 1996 Prionics or the kinetic basis of prion diseases. *Biophys. Chem.* **63**, A1–A18. (doi:10.1016/S0301-4622(96)02250-8)
61. Nowak MA, Krakauer DC, Klug A, May RM. 1998 Prion infection dynamics. *Integr. Biol.: Issues News Rev.* **1**, 3–15. (doi:10.1002/(SICI)1520-6602(1998)1:1<3::AID-INBI2>3.3.CO;2-0)
62. Kandel ER, Koester JD, Mack SH, Siegelbaum SA. 2021 *Principles of neural science*, 6th edn. Health Professions Division. New York, NY: McGraw-Hill.
63. Vilchez D, Saez I, Dillin A. 2014 The role of protein clearance mechanisms in organismal ageing and age-related diseases. *Nat. Commun.* **5**, 5659. (doi:10.1038/ncomms6659)
64. Patterson BW *et al.* 2015 Age and amyloid effects on human central nervous system amyloid-beta kinetics. *Ann. Neurol.* **78**, 439–453. (doi:10.1002/ana.24454)
65. Erban R, Chapman SJ. 2020 *Stochastic modelling of reaction–diffusion processes*. Cambridge Texts in Applied Mathematics. Cambridge, UK: Cambridge University Press.
66. Bateman RJ, Munsell LY, Morris JC, Swarm R, Yarasheski KE, Holtzman DM. 2006 Human amyloid-β synthesis and clearance rates as measured in cerebrospinal fluid in vivo. *Nat. Med.* **12**, 856–861. (doi:10.1038/nm1438)
67. Smith AF *et al.* 2019 Brain capillary networks across species: a few simple organizational requirements are sufficient to reproduce both structure and function. *Front. Physiol.* **10**, 1–22. (doi:10.3389/fphys.2019.00233)
68. Goirand F, Georgeot B, Giraud O, Lorthois S. 2021 Network community structure and resilience to localized damage: application to brain microcirculation. *Brain Multiphys.* **2**, 100028. (doi:10.1016/j.brain.2021.100028)
69. Wormald NC. 1999 Models of random regular graphs. In *Surveys in combinatorics, 1999* (eds JD Lamb, DA Preece), London Mathematical Society Lecture Note Series, pp. 239–298. Cambridge, UK: Cambridge University Press. (doi:10.1017/CBO9780511721335.010)
70. Pries AR, Secomb TW, Gaehtgens P, Gross JF. 1990 Blood flow in microvascular networks. Experiments and simulation. *Circ. Res.* **67**, 826–834. (doi:10.1161/01.RES.67.4.826)
71. Gavrilchenko T, Katifori E. 2019 Resilience in hierarchical fluid flow networks. *Phys. Rev. E* **99**, 012321. (doi:10.1103/PhysRevE.99.012321)
72. Newman M. 2018 *Networks*, 2nd edn. Oxford, UK: Oxford University Press.
73. Goirand F. 2021 Statistical modelling of blood flow and transport in brain micro-vascular networks. See https://theses.hal.science/tel-04170869v1/file/Goirand_Florian.pdf.

74. Kirkpatrick S. 1971 Classical transport in disordered media: scaling and effective-medium theories. *Phys. Rev. Lett.* **27**, 1–4. (doi:10.1103/PhysRevLett.27.1722)
75. Kirkpatrick S. 1973 Percolation ancl conduction. *Rev. Mod. Phys.* **45**, 574–588. (doi:10.1103/RevModPhys.45.574)
76. Britton NF. 1986 *Reaction-diffusion equations and their applications to biology*. New York, NY: Academic Press.
77. Nath S, Agholme L, Kurudenkandy FR, Granseth B, Jan M, Hallbeck M. 2012 Spreading of neurodegenerative pathology via neuron-to-neuron transmission of β-amyloid. *J. Neurosci.* **32**, 8767–8777. (doi:10.1523/JNEUROSCI.0615-12.2012)
78. Brahic M, Bousset L, Bieri G, Melki R, Gitler AD. 2016 Axonal transport and secretion of fibrillar forms of α-synuclein, Aβ42 peptide and HTTExon 1. *Acta Neuropathol.* **131**, 539–548. (doi:10.1007/s00401-016-1538-0)
79. Raj A, Kuceyeski A, Weiner M. 2012 A network diffusion model of disease progression in dementia. *Neuron* **73**, 1204–1215. (doi:10.1016/j.neuron.2011.12.040)
80. Raj A, LoCastro E, Kuceyeski A, Tosun D, Relkin N, Weiner M. 2015 Network diffusion model of progression predicts longitudinal patterns of atrophy and metabolism in Alzheimer's disease. *Cell Rep.* **10**, 359–369. (doi:10.1016/j.celrep.2014.12.034)
81. Raj A, Powell F. 2018 Models of network spread and network degeneration in brain disorders. *Biol. Psychiatry: Cogn. Neurosci. Neuroimaging* **3**, 788–797. (doi:10.1016/j.bpsc.2018.07.012)
82. Bullmore E, Sporns O. 2009 Complex brain networks: graph theoretical analysis of structural and functional systems. *Nat. Rev. Neurosci.* **10**, 186–198. (doi:10.1038/nrn2575)
83. Daducci A, Gerhard S, Griffa A, Lemkaddem A, Cammoun L, Gigandet X, Meuli R, Hagmann P, Thiran JP. 2012 The connectome mapper: an open-source processing pipeline to map connectomes with MRI. *PLoS ONE* **7**, e48121. (doi:10.1371/journal.pone.0048121)
84. Xia M, Wang J, He Y. 2013 BrainNet viewer: a network visualization tool for human brain connectomics. *PLoS ONE* **8**, 1–15. (doi:10.1371/journal.pone.0068910)
85. Putra P, Thompson TB, Chaggar P, Goriely A. 2021 Braiding Braak and Braak: staging patterns and model selection in network neurodegeneration. *Netw. Neurosci.* **5**, 929–956. (doi:10.1162/netn_a_00208)
86. Stumpf MP, Krakauer DC. 2000 Mapping the parameters of prion-induced neuropathology. *Proc. Natl Acad. Sci. USA* **97**, 10 573–10 577. (doi:10.1073/pnas.180317097)
87. Kouvaris NE, Sebek M, Iribarne A, Díaz-Guilera A, Kiss IZ. 2017 Stationary patterns in star networks of bistable units: theory and application to chemical reactions. *Phys. Rev. E* **95**, 1–8. (doi:10.1103/PhysRevE.95.042203)
88. Lojasiewicz S. 1963 Une propriété topologique des sous-ensembles analytiques réels. *Les équations aux dérivées partielles* **117**, 87–89.
89. Glendinning P. 1994 *Stability, instability and chaos: an introduction to the theory of nonlinear differential equations*. Cambridge, UK: Cambridge University Press.
90. Alzheimer A. 1898 Neuere Arbeiten über die Dementia senilis und die auf atheromatöser Gefässerkrankung basierenden Gehirnkrankheiten. *Monatsschr. Psychiatr. Neurol.* **3**, 101–115. (doi:10.1159/000228782)
91. Stakos DA, Stamatelopoulos K, Bampatsias D, Sachse M, Zormpas E, Vlachogiannis NI, Tual-Chalot S, Stellos K. 2020 The Alzheimer's disease amyloid-beta hypothesis in cardiovascular aging and disease: JACC focus seminar. *J. Am. Coll. Cardiol.* **75**, 952–967. (doi:10.1016/j.jacc.2019.12.033)
92. Laurent M. 1996 Prion diseases and the 'protein only' hypothesis: a theoretical dynamic study. *Biochem. J.* **318**, 35–39. (doi:10.1042/bj3180035)
93. Laurent M. 1997 Autocatalytic processes in cooperative mechanisms of prion diseases. *FEBS Lett.* **407**, 1–6. (doi:10.1016/S0014-5793(97)00310-4)
94. Garcia-Alloza M, Gregory J, Kuchibhotla KV, Fine S, Wei Y, Ayata C, Frosch MP, Greenberg SM, Bacskai BJ. 2011 Cerebrovascular lesions induce transient β-amyloid deposition. *Brain* **134**, 3694–3704. (doi:10.1093/brain/awr300)
95. Bannai T *et al.* 2019 Chronic cerebral hypoperfusion shifts the equilibrium of amyloid β oligomers to aggregation-prone species with higher molecular weight. *Sci. Rep.* **9**, 1–5. (doi:10.1038/s41598-019-39494-7)
96. Keener JP. 1987 Propagation and its failure in coupled systems of discrete excitable cells. *SIAM J. Appl. Math.* **47**, 556–572. (doi:10.1201/b16530)

97. Kouvaris NE, Kori H, Mikhailov AS. 2012 Traveling and pinned fronts in bistable reaction-diffusion systems on networks. *PLoS ONE* **7**, e45029. (doi:10.1371/journal.pone.0045029)
98. Kouvaris NE, Isele T, Mikhailov AS, Schöll E. 2014 Propagation failure of excitation waves on trees and random networks. *Epl* **106**, 68001. (doi:10.1209/0295-5075/106/68001)
99. Mawuenyega KG, Sigurdson W, Ovod V, Munsell L, Kasten T, Morris JC, Yarasheski KE, Bateman RJ. 2010 Decreased clearance of CNS β-amyloid in Alzheimer's disease. *Science* **330**, 1774. (doi:10.1126/science.1197623)
100. Fisher RA. 1937 The wave of advance of advantageous genes. *Ann. Eugeneics* **7**, 355–369. (doi:10.1111/j.1469-1809.1937.tb02153.x)
101. Henderson MX *et al.* 2019 Spread of α-synuclein pathology through the brain connectome is modulated by selective vulnerability and predicted by network analysis. *Nat. Neurosci.* **22**, 1248–1257. (doi:10.1038/s41593-019-0457-5)
102. Blinder P, Tsai PS, Kaufhold JP, Knutsen PM, Suhl H, Kleinfeld D. 2013 The cortical angiome: an interconnected vascular network with noncolumnar patterns of blood flow. *Nat. Neurosci.* **16**, 889–897. (doi:10.1038/nn.3426)
103. Ahern A, Thompson TB, Oliveri H, Lorthois S, Goriely A. 2025 Modelling cerebrovascular pathology and the spread of amyloid beta in Alzheimer's disease. Figshare. (doi:10.6084/m9.figshare.c.7700081)